Remote Sensing of Environment 331 (2025) 115039

Contents lists available at ScienceDirect

Remote Sensing of Environment

journal homepage: www.elsevier.com/locate/rse

Mapping and early warning of hidden landslides under forests: A case in Lantau, Hong Kong

Ziyuan Li [a], Guoqiang Shi [a,b,*], Songbo Wu [a,b], Tao Li [c], Zhong Lu [d], Xiaoli Ding [a]

[a] Department of Land Surveying and Geo-Informatics, Research Institute for Land and Space, The Hong Kong Polytechnic University, Hong Kong SAR, China
[b] Shenzhen Research Institute, The Hong Kong Polytechnic University, Shenzhen, China
[c] Land Satellite Remote Sensing Application Center, Beijing, China
[d] The Roy M. Huffington Department of Earth Sciences, South Methodist University, Dallas, TX 75275, USA

ARTICLE INFO

Edited by: Jing M. Chen

Keywords:
Small-scale landslides
Hong Kong
Lutan-1
Heterogeneous phase restoration
Extreme rainfall

ABSTRACT

The intensification of extreme rainfall has exacerbated widespread landslide hazards, particularly in tropic and subtropic regions. Hong Kong—the world's most densely populated city situated on steep, forested terrain—faces chronic landslide risks that are challenging to monitor with conventional Aperture Radar Interferometry (InSAR), as hillslope failures are typically small and hidden beneath dense canopy. This study develops a novel detection framework integrating: 1) HARMIE (Homogeneous Amplitude-phase RefineMent for local Inconsistent phase Estimation), which enhances localized phase variability for subtle displacement retention; and 2) a phase gradient-based detection approach, linking slope responses with extreme rainfall. Simulated and real-data experiments demonstrate that HARMIE outperforms conventional methods by better preserving localized phase detail and magnitude. Using high-resolution ascending and descending Lutan-1 (LT-1) SAR datasets (July 2023–October 2024) over Lantau Island, Hong Kong, the framework mapped widespread hillslope failures triggered by the October 2023 extreme rainfalls, achieving a 27 % higher recognition rate than amplitude-homogeneity-based detection, with notable improvements in capturing subtle failures as narrow as ~10 m. Ten active landslides concealed beneath forests were also pinpointed. Beyond detection, our analysis reveals that prolonged antecedent rainfall drives seasonal progressive creep on minor slopes and, for certain slopes, may interact with extreme rainfall to accelerate destabilization. This study represents the first InSAR-based mapping of small, forest-covered landslides in Hong Kong using L-band SAR, offering new insights into hillslope destabilization in forested mountainous terrain and advancing the development of landslide early-warning systems in such regions.

1. Introduction

Landslides pose a persistent and significant threat in Hong Kong due to its steep terrain, widespread presence of geologically susceptible materials, and the impact of intense tropical monsoon rainfall (Brand et al., 1984). Particularly during extreme rainfall events, the excessive moisture within superficial, loose soil mantle that is extensively distributed across Hong Kong, often leads to transient hillslope failures (Dai et al., 1999; Dai and Lee, 2002; Lu and Godt, 2013). The increasing frequency and intensity of extreme precipitation have further exacerbated the risk of hillslope failures in the region (Lai et al., 2024). For instance, two recent extreme rainfall events—on June 7, 2008 (maximum hourly rainfall of 145.5 mm recorded at the Hong Kong Observatory, HKO) and September 7, 2023 (maximum hourly rainfall of 158.1 mm)—triggered 362 and 214 landslides, respectively, resulting in casualties, extensive infrastructure damages, and substantial economic losses. Proactive landslide mapping and early detection of hillslope movements are crucial for geohazard management and mitigating in this densely built and populated city.

Synthetic Aperture Radar Interferometry (InSAR) has been widely applied for landslide mapping and demonstrates its superiority in geohazard early warning through the detection of active slope instability (Chen et al., 2025; Handwerger et al., 2019; Zheng et al., 2024). In vegetated regions, where significant decorrelation contaminates

* Corresponding author at: Department of Land Surveying and Geo-Informatics, Research Institute for Land and Space, The Hong Kong Polytechnic University, Hong Kong SAR, China.
E-mail address: guoqiang.shi@polyu.edu.hk (G. Shi).

https://doi.org/10.1016/j.rse.2025.115039
Received 29 May 2025; Received in revised form 20 August 2025; Accepted 17 September 2025
Available online 27 September 2025

coherent signals of InSAR, noise reduction is commonly addressed through homogeneous multilooking and phase linking, which aggregate homogeneous pixels within neighborhoods to estimate optimum phase series (Ferretti et al., 2011; Shi et al., 2022b). These approaches reduce interferometric speckle and facilitate the effective retrieval of geophysical parameters (Ansari et al., 2018; Ferretti et al., 2011). To extract slope deformation from the optimum phase estimates, a common strategy involves time series post-processing, although this process is often hindered by unwrapping errors and significant atmospheric artifacts (Shi et al., 2022a; Wu et al., 2022). As an alternative, the phase gradient method circumvents the need for phase unwrapping by computing spatial differences between adjacent pixels, which can suppress long-wavelength atmospheric effects and enhance the delineation of deformation boundaries (Cao et al., 2023; Hu et al., 2020). The InSAR methods presented here offer promising solutions for unveiling ongoing landslide hazards in Hong Kong.

However, specific landslide features and challenging environmental conditions in Hong Kong significantly complicate the application of InSAR in tracking hillslope movements (Shi et al., 2022a, 2022b). The hilly terrain of Hong Kong is extensively mantled with shallow colluvial deposits (Brand et al., 1984; Dai and Lee, 2002). Due to their highly loose and permeable nature, these materials are prone to transient saturation under intense or extreme rainfall, triggering strong hydraulic responses and rendering the hillslopes susceptible to shallow destabilization (Brand et al., 1984; Dai et al., 1999; Dai and Lee, 2002; Lu and Godt, 2013). Most documented slope failures occur within these thin colluvial covers and frequently manifest as debris flows, a common failure mode in the region (Dai et al., 1999; Wong et al., 1998). Consequently, landslides in Hong Kong are predominantly characterized by shallow, channelized hillslope slips, typically with source widths of less than 20 m and failure depths of less than 3 m (Dai et al., 1999; Dai and Lee, 2002; Wong et al., 1998). Additionally, as in many tropical and subtropical regions, Hong Kong's hilly landscape is extensively forested. Dense vegetation leads to severe decorrelation, making the slipping signals of hillslopes difficult to detect. Whether due to visual obscuration by a dense canopy or coherence loss in InSAR, the signatures of small-scale landslide, such as subtle ground deformation or scarps, are often deeply hidden from observations. This challenge limits InSAR's ability to fully exploit its technical advantages.

When applied to detecting small-scale landslide signals in vegetated areas, current InSAR methods encounter the following difficulties. Conventional homogeneous multilooking using amplitude homogeneity does not inherently account for phase variability and therefore struggles to select homogeneous pixels for preservation of such localized phase associated with minor, small-scale hillslope movements. Under the canonical assumption of circularly symmetric complex Gaussian (CCG) distribution, the complex covariance matrix Σ of a Distributed Scatterer (DS) is considered a sufficient statistic for characterizing the SLC SAR vector and is used to infer the optimal phase history. In practice, the maximum likelihood estimate (MLE) of Σ is typically derived from a neighborhood of pixels selected based on amplitude homogeneity, serving as a proxy for the true matrix (Ansari et al., 2018; Ferretti et al., 2011; Goodman, 1963; Guarnieri and Tebaldini, 2008). The argument of the estimated Σ yields the multi-looked interferometric phase. However, incorporating spatially phase-inconsistent pixels into this estimation introduces bias, leading to an underestimated or overly smoothed phase and the loss of critical localized phase variations tied to small-scale landslides. Alternatively, some studies select homogeneous pixels based on interferometric phase similarity (Pepe et al., 2021; Yao and Balz, 2024). While this phase-based selection better preserves local phase heterogeneity, it violates the assumption of identical CCG distributions required for valid MLE of Σ. As a result, such approaches can still bias the coherence matrix estimation. Whether using amplitude- or phase-based methods, the neglect of spatial heterogeneity in either signal component compromises the accuracy of Σ estimation (Zwieback and Meyer, 2021). These biases ultimately degrade the reliability of phase linking and reduce the effectiveness of interferometric phase analysis in detecting small-scale hillside movements in Hong Kong. In the context of landslide mapping, the phase gradient approach generally involves stacking spatial gradient estimates in various forms to enhance the delineation of slope slipping extents (Cao et al., 2023; Hu et al., 2020; Zhang et al., 2024). While effective for identifying landslides across a large area, this approach remains limited in forested regions, where severe decorrelation disrupts phase continuity and obscures landslide boundaries—constraining its applicability primarily to sparsely vegetated terrain (Cao et al., 2023).

Therefore, advancements beyond the existing approaches are highly needed to meet the growing demands of detecting landslide-prone zones in Hong Kong and other similarly complex environments. First, enhancing the selection of homogeneous pixels—particularly by advancing methods to enable better preservation of localized phase heterogeneity during optimal phase estimation—can significantly improve the detection of weak landslide signals. In addition, the unique hydromechanical responses of hillslopes to extreme precipitation events offer valuable diagnostic cues. By jointly utilizing the hillslope kinematic characteristic and the temporal evolution of phase gradients, it becomes plausible to detect landslide-prone points, even where ground deformation signals are partially obscured. The availability of various L-band SAR datasets further supports this effort. In particular, the recent launch of the Lutan-1 (LT-1) SAR satellite, with its high spatial resolution (3 m) and long-wavelength capability, offers a valuable tool for reducing vegetation-induced decorrelation and detecting subtle, small-scale ground deformations.

In this study, we aim to extend the effectiveness of InSAR for mapping widespread and hidden landslides under forests. The Lantau Island in Hong Kong, with steep, densely forested terrain prone to landslide risks, is picked as the study area. LT-1 L-band SAR datasets from both ascending and descending orbits is used to minimize geometrical distortions. To detect the small-scale hillslope displacements from LT-1 interferograms, we propose a new method that selects hybrid homogeneous pixels from amplitude and phase attributes and harmonize their contribution for better approximating the MLE of Σ for optimal phase history recovery. This approach mitigates the significant decorrelation while preserving local phase heterogeneity to ensure the subtle slope moving signals are not submerged. We then quantitatively correlate the consecutive phase gradients with extreme rainfall intensities within each inter-acquisition period, identifying spatially clustered locations prone to hillslope movement. Ultimately, this proposed framework enables the mapping of landslide-prone areas across vast forested areas, proactively locate hidden but active sliding hillslopes and supports hazard mitigation planning in anticipation of future extreme rainfall events.

2. Study area and data

2.1. Study area

Lantau Island, the largest outlying island of Hong Kong, is situated in the southwestern part of the territory. Fig. 1 shows the graphical location of Lantau Island, in which the dot dashed line gives its outline. The island terrain is predominantly mountainous with significant elevation differences. A considerable portion of the hills exceeds 400 m in height, and many slopes are steeper than 25°, with the highest peak reaching 934 m. Due to its rugged topography, urban development on Lantau is mainly confined to relatively flat coastal areas, particularly along the northern shoreline where the Tung Chung area connects with the Hong Kong International Airport. The central mountainous region remains largely undeveloped and uninhabited. Vegetation cover on these slopes varies by elevation: the footslopes are abundant with densely forested, while the midslopes are typically covered with thick shrubs and grasslands. Geologically, the island is primarily composed of two rock types—volcanic rocks and granites. Volcanic rocks predominate the western

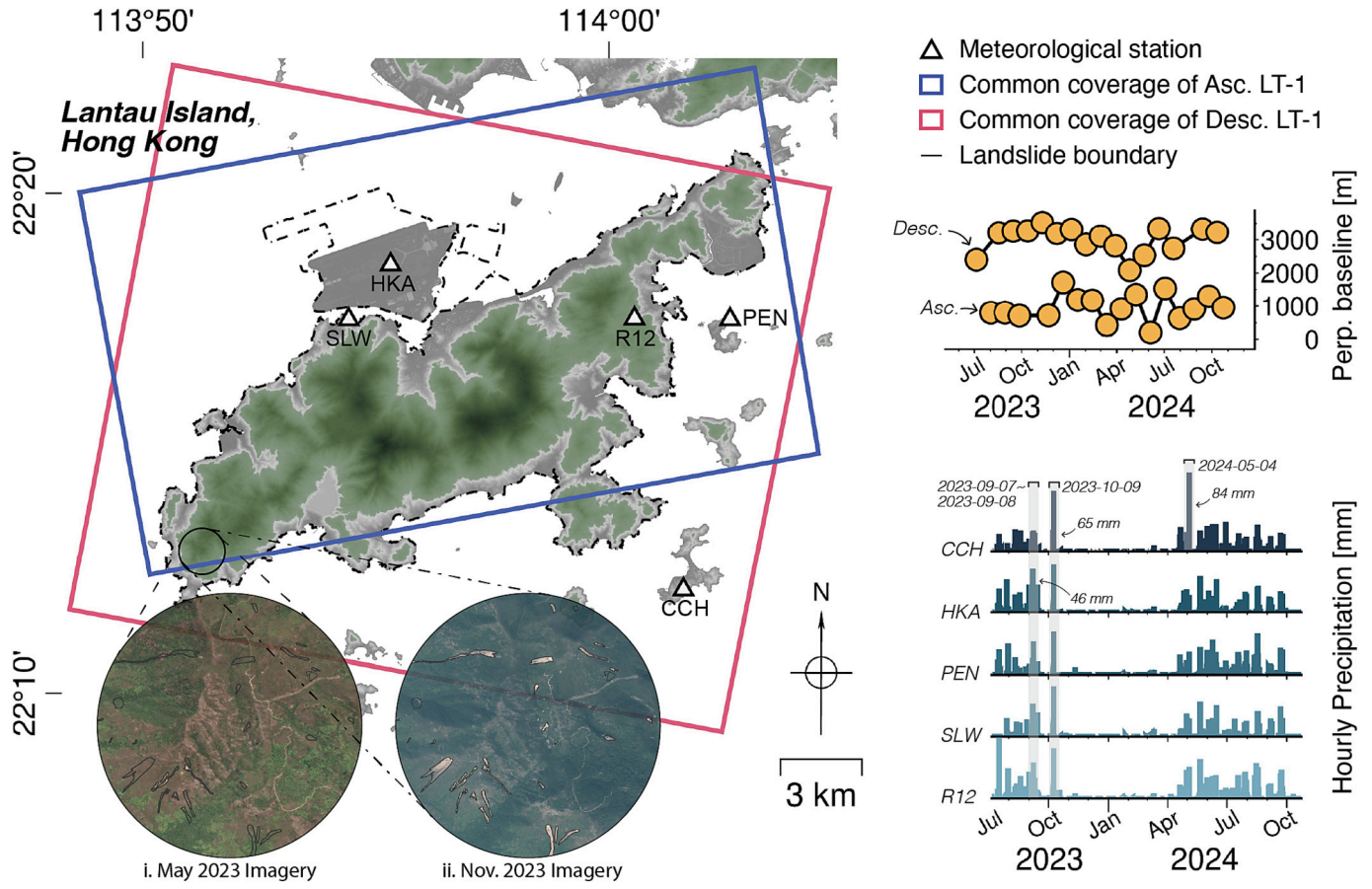

Fig. 1. Extent of the study area, delineated by the dash-dotted boundary of Lantau Island and superimposed on the LiDAR-derived topographic map. Circular insets show optical imageries highlighting newly formed hillslope failures after the extreme rainfall. Red and blue boxes denote the coverage areas of the descending and ascending LT-1 datasets, respectively. Their baseline histories are shown in the top-right plot. Triangles across Lantau Island mark meteorological stations used in the study, with corresponding hourly rainfall data displayed in the bottom-right panel. (For interpretation of the references to colour in this figure legend, the reader is referred to the web version of this article.)

two-thirds of Lantau Island, while granitic rocks are mainly distributed in the eastern third (Dai and Lee, 2002). Long-term weathering and erosion processes have led to the development of widespread shallow colluvial mantles over the hilly terrain, contributing to the geological vulnerability of the hillslopes.

Hillslope failures on Lantau often occur within thin colluvial deposits on steep hillslopes. These landslides are typically shallow (failure depths generally less than 3 m) and small in scale, often manifesting as debris flows that affect areas ranging from a few to several tens of meters (Dai and Lee, 2002; Wong et al., 1998). Under the impact of subtropical monsoonal climate of Hong Kong, the island experiences intense and concentrated rainfall during the summer months. This climatical condition, coupled with its steep terrain and weak slope stability, makes the hillslopes highly susceptible to landslides. In recent decades, the increasing frequency and intensity of extreme rainfall events have further exacerbated the risk of hillslope failures (Lai et al., 2024). Since the rapid urbanization in Hong Kong has led to dense development of buildings close to hillslopes, any slope failure occurring near these densely populated areas could lead to catastrophic consequences, therefore emphasizing the critical significance of this study.

2.2. LT-1 and LiDAR data

We utilized 16 ascending and 16 descending LT-1 SAR acquisitions, respectively. The images span the period from July 5, 2023, to October 11, 2024 (descending), and August 2, 2023, to October 23, 2024 (ascending). These acquisitions coincide with a period of LT-1 satellite orbital adjustment, resulting in limited overlap in the common imaging area—particularly for the ascending track, which does not fully cover Lantau Island (see left panel in Fig. 1). The baseline histories for both descending and ascending datasets are illustrated in the top-right corner of Fig. 1, with detailed baseline information provided in Table S4 of the supplementary material.

The stacks of LT-1 SAR Single Look Complex (SLC) data from both orbits were generated and coregistered. A high-resolution (5 m) Digital Surface Model (DSM), produced from LiDAR data collected in 2020, was collected from https://sdportal.cedd.gov.hk/#/en/ to ensure accurate removal of topographic phase components and to facilitate masking of areas affected by severe geometric distortions. This DSM, which fully covers Lantau Island, is also used for downslope deformation modelling.

2.3. Precipitation records and landslide imagery

Hourly precipitation data for the LT-1 revisiting period were obtained from the HKO for five meteorological stations on Lantau Island. The locations of these stations are shown as triangles in Fig. 1, together with plots of their hourly rainfall records right in the panel. Overall, the stations exhibited consistent rainfall pattern, with precipitation primarily concentrated in the summer months. During September–October 2023, two tropical cyclones, Typhoon Haikui and Typhoon Koinu, prominently affected the study area. According to HKO, cumulative rainfall exceeded 400 mm and 300 mm, respectively, across most parts of Hong Kong during the two events. On Lantau Island, the highest hourly rainfall during Typhoon Haikui reached 46 mm at HKA, while

Typhoon Koinu produced a peak of 65 mm at CCH. Compared to Typhoon Koinu, Typhoon Haikui had a more limited impact on Lantau Island. A severe rainfall event on 4 May 2024 produced a maximum hourly rainfall of 84 mm at CCH on Cheung Chau. According to the HKO's Weather Summary for May 2024 (https://www.hko.gov.hk/en/wxinfo/pastwx/mws2024/mws202405.htm), the storm had a greater impact on western Lantau and Cheung Chau. The availability of rainfall data from CCH therefore fills the gap left by the absence of a rainfall station in western Lantau, enabling analysis of this rainstorm event's impact on hillslope instability in the area.

Two sets of optical imagery of Lantau Island, acquired before and after the September–October typhoon events, were used to capture newly emerged hillslope failures induced by intense rainfall (typical areas are highlighted by the amplifiers in Fig. 1i and ii). The pre-event imagery is a Maxar WorldView-2 scene acquired on 30 May 2023 (World Imagery map, version dated 2024-06-06), while the post-event imagery is a November 2023 True Digital Orthophoto (TDOP) obtained from the CSDI portal (https://portal.csdi.gov.hk/csdi-webpage/). Comparing the two datasets enables precise identification of hillslope failures and delineation of their extents, providing ground-truth references for validating subsequent phase retrieval and landslide detection results. In total, 89 landslide failures were confirmed, with their

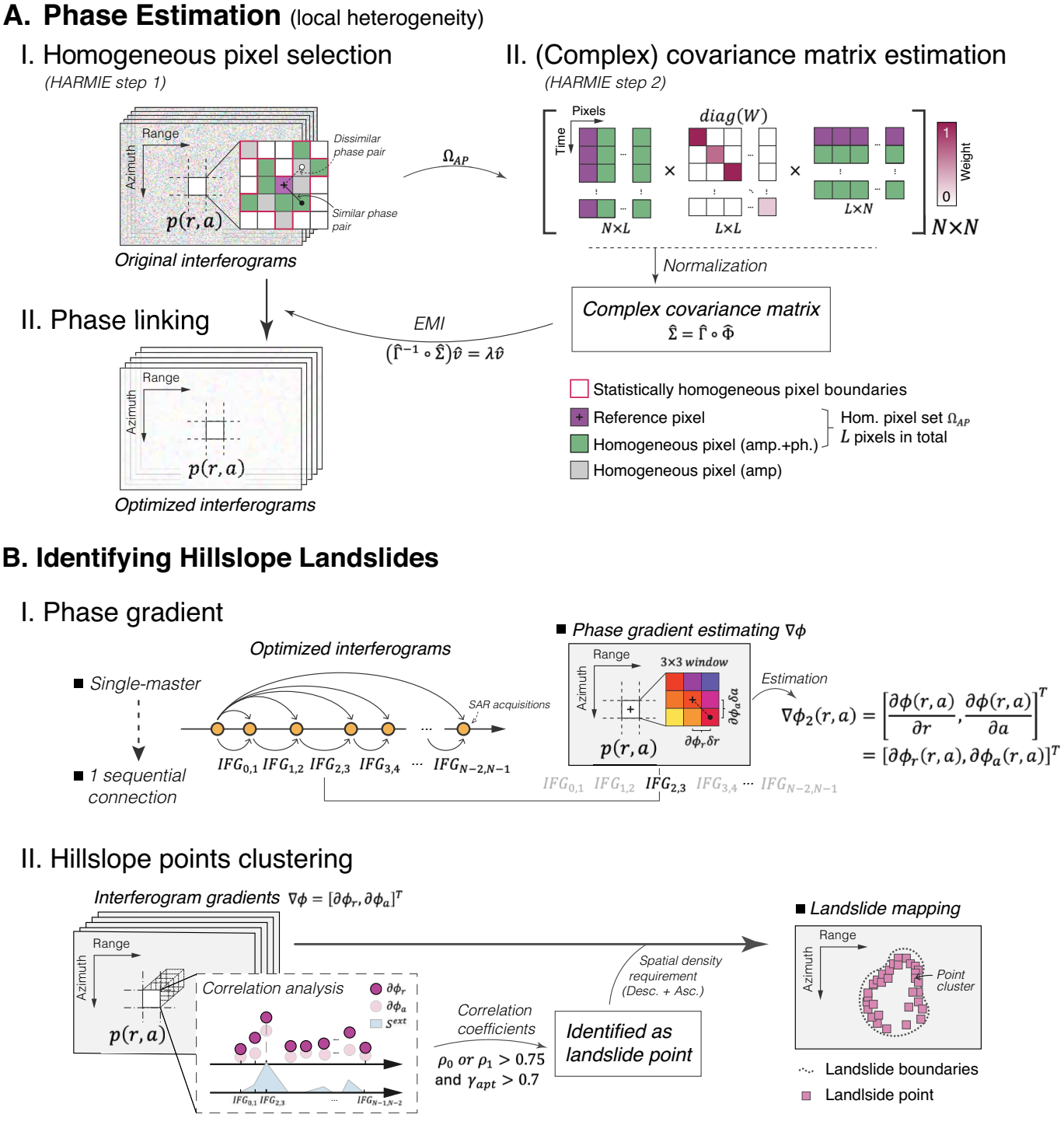

Fig. 2. The workflow of the proposed landslide detection framework.

geographical coordinates listed in Table. S5 and their boundary delineations (solid black line) presented alongside the results in subsequent sections.

3. Methodologies

Fig. 2 summarizes research framework of this study. Prior to detailing the methodologies, we first establish the mathematical symbols adopted throughout this paper. Given N SAR acquisitions, let $\mathscr{Z}_0 = \{0, 1, \ldots, N-1\}$ denote the discrete set of SAR scene indices, where each integer $i \in \mathscr{Z}_0$ corresponds to a unique SAR acquisition timestamp. We define an auxiliary index set $\mathscr{Z}_1 = \{0, 1, \ldots, N-2\}$, to label the consecutive interferometric pairs generated from adjacent SAR scenes (i.e., the k-th interferogram is formed by scenes k and $k+1$ for $k \in \mathscr{Z}_1$).

3.1. Retrieval of optimal phase history

3.1.1. SAR/InSAR statistics

A. Coherence matrix biasing

In canonical formulation of MLE phase linking, the quality of phase estimation is highly dependent on the accuracy of the coherence matrix estimate, $\widehat{\Gamma} = |\widehat{\Sigma}|$. As discussed in Section 1, reliance on amplitude or phase homogeneity alone risks incorporating pixels with inconsistent phase or amplitude into sample set, consequently introducing bias into $\widehat{\Sigma}$ that distorts phase series estimates subsequently. This section justifies the need for refined homogeneous pixel selection through qualitative and quantitative analysis of the bias in Γ estimate when relying solely on amplitude or phase homogeneity.

Suppose a complex vector $\xi \in \mathbb{C}^N$ from a generic DS in a stack of N co-registered single look complex (SLC) SAR images. Complex covariance matrix $\Sigma \in \mathbb{C}^{N \times N}$ is defined by the ensemble expectation of Hermitian product of ξ. It is typically normalized to ensure $E(\xi_i^2) = 1$, which enables the factorization:

$$\Sigma = E(\xi\xi^H) = \Gamma \circ \Phi \tag{1}$$

where H and $\circ$ denote Hermitian transpose and Hadamard product, respectively. Γ represents coherence matrix, magnitude of Σ, and Φ contains interferometric phases ϕ_{mn} of all possible pairs, with the entry of $\exp(j\phi_{mn})$, $m, n \in \mathscr{Z}_0$. Under the assumption of CCG distributed DS, amplitude-based approach ensures selected neighboring pixels reaching statistical homogeneity in SLC samples (Ferretti et al., 2011; Goodman, 1963; Hanssen, 2001). The MLE $\widehat{\Sigma}$ of Σ can be thereafter derived via Hermitian products over homogeneous samples. Then, $\widehat{\Gamma} = |\widehat{\Sigma}|$ serves as a sufficiently approximate coherence matrix for inferring optimal phase series (Ansari et al., 2018; Ferretti et al., 2011).

For small-scale landslide monitoring, where localized phase inconsistency arises, multilooked interferometric phases in the argument of $\widehat{\Sigma}$ will be underestimated. Amplitude-based methods select amplitude-homogeneity pixels but risk including SLC vectors with divergent orientations, reducing the magnitude of the averaged vector and thus attenuating $\widehat{\Gamma}$. Phase-based approaches, conversely, impose no constraints on amplitude homogeneity that results in the selected pixels consisting of dispersed amplitude samples, similarly, leading to an underestimated $\widehat{\Gamma}$.

To assess the underestimation described above, we conducted Monte Carlo simulations (Samiei-Esfahany et al., 2016), considering three scenarios: (1) fully homogeneous set, of which amplitude and phase samples are drawn from i.i.d. probability density function (p.d.f.), (2) with 30 % phase heterogeneity, (3) with 30 % amplitude heterogeneity. Specific simulation parameters and result analysis are provided in the supplementary material (Section S1.2). As shown in Fig. 3, the fully homogeneous set yielded coherence estimates with minor positive bias

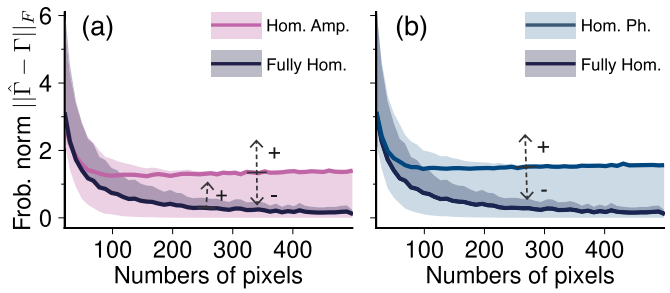

Fig. 3. Estimation bias of the coherence matrix $\|\widehat{\Gamma} - \Gamma\|_F$ (Frobenius norm between estimated and true values) under amplitude-only (Hom. Amp.), phase-only (Hom. Ph.), and fully homogeneous (Fully Hom.) scenarios. (a, b) The dark magenta, navy blue, and black solid lines represent the estimation biases under amplitude, phase, and fully homogeneous conditions, respectively, as homogeneous pixel number increases. As indicated by the dashed arrows, the shaded areas above and below each solid line represent the magnitude of positive and negative estimation biases, respectively. (For interpretation of the references to colour in this figure legend, the reader is referred to the web version of this article.)

(gray shadow above the solid black line) that converged with increasing sample size, consistent with previous findings (Touzi et al., 1999). In contrast, the inclusion of phase or amplitude heterogeneity introduced larger deviations and potential underestimation of coherence (red and blue shadows below the corresponding red and blue solid lines) as sample size grows. These findings underscore the critical need for rigorous homogeneous pixel selection to minimize coherence estimation bias.

B. Phase similarity statistic

The phase of a SLC pixel is inherently disordered within the 2π interval and is statistically characterized by uniform distribution (Hanssen, 2001). When two coherent SAR variables are conjugately multiplied to form interferometric phase, the resulting distribution becomes cyclically symmetric and concentrated, because of the cancellation of common noisy components and the amplification of coherent signals (Just and Bamler, 1994; Samiei Esfahany, 2017). As coherence decreases, the interferometric phase distribution progressively approaches uniformity, resembling the randomness of SLC phases. To better access local phase similarity, the spatial differential interferometric phase between reference p_0 and its neighbor p_1 is computed as $\delta\phi = \langle \phi_1 - \phi_0 \rangle_{-\pi,\pi}$, where $\langle \bullet \rangle_{-\pi,\pi}$ is the modulo-2π operator within the range $[-\pi, \pi]$. This operation cancels shared phase components between pixels and retains only local heterogeneous contributions, thereby making $\delta\phi$ suitable evaluating inter-pixel phase similarity.

Here, we demonstrate the shape and distributional characteristics of $\delta\phi$ supports quantifying inter-pixel phase similarity. Assuming that p_0 and p_1 are at least moderately coherent and possess multi-baseline interferometric phase observations, the distribution of $\delta\phi$ would also exhibit cyclical symmetry and concentration. The shape of the distribution reflects the combined effects of low-pass and high-pass components: the former predominantly encompasses displacement and height-related differences at local scale that shift the symmetry axis of the distribution (typically from 0 to $|\pi|$), while the latter, dominated by decorrelation, affects the degree of concentration. When $\delta\phi$ is represented as a unit vector in a complex plane, the low-pass components determine the principal orientation of the distribution, exhibiting directionality, whereas the high-pass components influence its spread within $[-\pi, \pi]$, dependent on joint decorrelating behaviors of p_0 and p_1. It can be inferred that a tight clustering of $\delta\phi$ samples around zero suggests a high phase similarity between p_0 and p_1. In contrast, shifted orientation and increased dispersion reduce phase similarity but with distinct ways. When decorrelation of any pixel dominates interfero-

metric phase, the distribution reduces to uniformity. As such, $\delta\phi$ can serve as a sensitive indicator of phase variation of a neighboring pixel relative to its local reference, making it a useful metric for quantifying phase homogeneity.

Given the angular essence and the directionality of $\delta\phi$, it can be approximately modeled by unimodal, symmetric Von Mises (VM) distribution (Mardia and Jupp, 2000):

$$g(\vartheta;\mu,\kappa)=\frac{1}{2\pi I_0(\kappa)}e^{\kappa\cos(\vartheta-\mu)} \tag{2}$$

where ϑ denotes directional variable, represented by $\delta\phi$ in the study, and $I_0(\bullet)$ denotes the zero-order modified Bessel function of the first kind. $\mu\in[-\pi,\pi]$ is the mean direction that indicates the symmetrical axis of ϑ distribution. κ is concentration parameter $(\kappa>0)$, with the value increasing to infinity meaning a highly concentrated distribution of ϑ, whereas the distribution reduces to be uniform as κ close to 0. Given M samples for the circular variable ϑ, the MLE $\widehat{\mu}$ of μ is the argument of arithmetic averaging of the unit phasors $\widehat{\mu}=\angle\left(\frac{1}{M}\sum e^{j\vartheta}\right)$. The magnitude of this average, $\overline{R}=\left|\frac{1}{M}\sum e^{j\vartheta}\right|, 0\le\overline{R}\le 1$, known as the mean resultant length, measures the concentration of circular data. From this, the sample circular variance is calculated as $V=1-\overline{R}, 0\le V\le 1$. The concentration parameter κ can be estimated from $\overline{R}$ using an approximation (see Eq. S6). We demonstrate and verify the VM distribution's fitting performance on $\delta\phi$ of distributed scatterers (DSs) in Fig. S1.

As stated previously, a sharply concentrated distribution of $\delta\phi$ around zero ($\mu=0$ with significantly large κ) indicates strong phase similarity between two pixels, interpreted here as phase homogeneity. By relaxing this strict criterion, pixel pairs are regarded as minimally phase-similar provided that the $\delta\phi$ distribution is statistically distinct from a uniform distribution without requiring $\mu=0$. We define this relaxed condition as phase quasi-homogeneity, which allows inclusion of a broader set of pixels while still preserve a minimum level of phase similarity with p_0.

3.1.2. Homogeneous pixel selection and phase estimation

To address the challenges of detecting small-scale, slow-moving signals in forested hillslopes, we propose a method called Homogeneous Amplitude-phase RefineMent for local Inconsistent phase Estimation (HARMIE). The method begins by identifying candidate homogeneous pixels, Ω_A, using a conventional amplitude-based approach. These candidates are then refined based on phase quasi-homogeneity, resulting in a refined set Ω_{AP}, which better tracks local phase variability. Residual phase heterogeneities between the reference pixel p_0 and its neighbors within Ω_{AP} are subsequently harmonized to improve $\widehat{\Sigma}$ estimation. The HARMIE implementation procedures are overviewed in Fig. 2A (I-II).

A. Amplitude homogeneous pixels Ω_A

To enable the MLE of the covariance matrix Σ, SLC observations must be drawn from a homogeneous pixel set that follows an i.i.d. CCG distribution. The first step is to construct an initial candidate set Ω_A based on amplitude homogeneity. Several established methods exist for this purpose, most of which rely on hypothesis testing (Ferretti et al., 2011; Jiang et al., 2015; Parizzi and Brcic, 2011). In this study, the specific amplitude-based method is selected considering SAR data availability and computational efficiency (Samiei-Esfahany and Hanssen, 2017). For instance, Kolmogorov-Smirnov method is suitable for medium size of SAR stacks in the study's simulation experiment (Ferretti et al., 2011; S. Samiei Esfahany, 2017), while given that only 16 LT-1 SAR images are available per orbit and each image contains a large number of pixels, Rayleigh distribution test based on Generalized Likelihood Ratio Test (GLRT) is more appropriate (Parizzi and Brcic, 2011; S. Samiei Esfahany, 2017). In both cases, a false alarm rate of 0.05 is adopted. Based on this, candidate homogeneous set Ω_A is constructed around p_0.

B. Phase quasi-homogeneity refinement on Ω_A

Phase homogeneity used to optimize the initial amplitude-based homogeneous pixel set Ω_A can ensure the accuracy of sample selection. However, strict selection criterion often results in a significantly reduced effective sample size, increasing the risk of biasing $\widehat{\Gamma}$ (Fig. 3). To address this, a phase quasi-homogeneity strategy is developed to refine pixels within Ω_A that at least exhibit minimal phase similarity.

To improve the sampling of phase observations and reduce the dominance of decorrelation in phase measurements caused by long temporal baselines, we reformulate the original data ϕ into a series of n-connected interferometric pairs. For a total of N SAR acquisitions, this method generates $n(2N-n-1)/2$ interferograms, significantly increasing the number of phase samples available. This enhanced sample size strengthens the reliability of similarity testing. In this study, four sequential connections were applied to the LT-1 datasets, yielding a total of 54 interferometric observations, adequate for robust statistical testing. The interferometric network can also be tailored to the specific study case, for example, to clearly resolve ground rupture boundaries induced by seismic activities. Next, observation arcs between the reference pixel p_0 and salve pixels in Ω_A are formed, and the corresponding spatial interferometric phase differences $\delta\phi$ are calculated. At this point, $\delta\phi$ quantifies the phase difference of the slave pixel relative to the reference pixel. These (wrapped) phase differences are modeled using the VM distribution to characterize their directional statistics and refine the selection of phase quasi-homogeneous pixels from Ω_A.

Let the interferometric phase difference $\delta\phi$ assigned to the directional variant ϑ in the VM's p.d.f. (Eq. 2). By testing the uniformity of the $\delta\phi$ distribution, we exclude pixels with completely dissimilar phase behavior while retaining those showing concentrated (albeit possibly shifted) distributions. This process is implemented employing the Rayleigh test, a score-based test for the uniformity of the VM distribution. Under the null hypothesis of uniformity (i.e., $\kappa=0$), the VM distribution simplifies to a uniform distribution. The simplified Rayleigh score statistic S is given by (see supplementary material for derivation) (Mardia and Jupp, 2000):

$$S=2n\overline{R}^2\sim\chi_2^2 \tag{3}$$

asymptotically following chi-square distribution χ_2^2 with 2 degrees of freedom. The slave pixels whose $\delta\phi$ distribution is not significantly distinct from uniform distribution at a 0.2 significance level are retained as phase-similar to form the refined spatial domain Ω_{AP}. This approach allows for the maximization of usable samples while preserving phase similarity, without relying on directly asymptotical estimation of the shape parameter κ (Eq. S6), which can be error-prone under limited samples or decorrelated conditions.

C. Harmonizing Ω_{AP} for coherence matrix estimation and phase estimation

In comparison with the rigor of amplitude homogeneity within pixels, phase quasi-homogeneity for defining Ω_{AP} is more relaxed, allowing a certain degree of phase dissimilarity relative to p_0, as discussed in Section 3.1.1. From the perspective of $\delta\phi$ distribution, such heterogeneity possibly causes a shift in the mean direction μ and/or lead to a more flattened distribution, resulting in a departure from ideal homogeneity. To address this, phase heterogeneity weighting is applied to harmonize the residual imbalances between p_0 and its neighbors $\{p_k\}_{k=1}^{L-1}$ within Ω_{AP}, emphasizing phase contributions more similar to p_0. We introduce a dispersion measure D_α that quantifies the angular spread of ϑ around a reference angle α (Mardia and Jupp, 2000)

$$D_\alpha = V + 2\overline{R}\left[\sin\left(\frac{\overline{\vartheta}-\alpha}{2}\right)\right]^2 \tag{4}$$

Here, the first term V reflects the overall angular dispersion of $\delta\phi$ within the interval of $[-\pi,\pi]$. When $\alpha = 0$ and $\widehat{\mu}$ assigned to $\overline{\vartheta}$ forming D_0, the second term measures the deviation of mean direction $\widehat{\mu}$ from zero. That is, D_0 captures both the noise-induced spread and the dominant phase shift, providing a comprehensive quantification of the phase dissimilarity between each neighboring pixel p_k and reference p_0.

Accordingly, this measure is used to construct a set of weights $\left[w_l = 1/D_0^{(l)}\right]_{l=1}^{L-1}$ for neighboring pixels, while determining the optimal value of reference weight $w_0 = 1/D_0^{(0)}$ for p_0 will be discussed in Section 4.1.1.. Currently, assuming $D_0^{(0)}$ is known, a complete weight column vector is defined as $W = \left[1/D_0^{(l)}\right]_{l=0}^{L-1}$. Then, the weighted covariance matrix estimate is computed as:

$$\widehat{\Sigma}_{ik} = \frac{\sum_{l=0}^{L-1} Z_{il} w_l Z_{kl}}{\sqrt{\sum_{l=0}^{L-1}|Z_{il}|^2 w_l |Z_{kl}|^2}} = \widehat{\gamma}_{ik} e^{j\widehat{\phi}_{ik}} \tag{5}$$

where $\widehat{\gamma}_{ik}$ and $\widehat{\phi}_{ik}$ represent the sample coherence magnitude and the corresponding multi-looked interferometric phase for the ik-th pair. This phase-adaptive estimation constitutes the final step of the HARMIE method, enhancing coherence matrix accuracy by harmonizing residual phase heterogeneity between reference and its neighboring pixels in Ω_{AP}. The optimum phase $\widehat{\phi}$ is estimated via EMI estimator (Ansari et al., 2018):

$$\left(|\widehat{\Sigma}|^{-1} \circ \widehat{\Sigma}\right)\widehat{v} = \lambda \widehat{v} \tag{6}$$

where λ is the minimum eigenvalue of the Hadamard product $|\widehat{\Sigma}|^{-1} \circ \widehat{\Sigma}$, and $\widehat{v}$ is the corresponding eigenvector from which optimal phase estimate $\widehat{\phi}$ is extracted. Then, a posteriori coherence map γ_{apt} is accordingly produced to assess goodness-of-fit of $\widehat{\phi}$, supporting subsequent phase gradient retrieval (Ansari et al., 2018; Ferretti et al., 2011).

3.2. Landslide identification

3.2.1. Retrieving interferogram gradients

Deformation mapping relying on time series InSAR analysis are often compromised by phase unwrapping errors and atmospheric disturbances (Cao et al., 2023; Hu et al., 2020). These challenges are particularly acute in our study area due to strong atmospheric activity in the coastal and mountainous environment (Shi et al., 2022a). To mitigate the disturbances, we employ a phase gradient approach using optimized LT-1 interferograms, which bypasses unwrapping errors and long-wavelength atmospheric effects while highlights sliding deformation boundaries on hillsides. This is further enhanced by incorporating phase results derived from the HARMIE approach, which preserves local phase sharpness for finer detection of landsliding.

Rather than directly computing phase differences between neighboring pixels along range r and azimuth a directions in the ith interferogram, we estimate the phase gradients $\nabla\phi(r,a,i) = \left(\frac{\partial\phi(r,a,i)}{\partial r}, \frac{\partial\phi(r,a,i)}{\partial a}\right)^T$, exploiting local phase information (Parizzi, 2020; Ross et al., 2024). This is an approximation method that assumes $\nabla\phi(r_0,a_0,i)$ is locally stationary around a pixel (r_0,a_0), and a first-order Taylor-series expansion is applicable. Surrounding a pixel of (r_0,a_0), the phase $\phi(r,a,i)$ at (r,a) can be modeled as:

$$\begin{aligned}\phi(r,a,i) &\approx \frac{\partial\phi(r_0,a_0,i)}{\partial r}(r-r_0) + \frac{\partial\phi(r_0,a_0,i)}{\partial a}(a-a_0) + \phi(r_0,a_0,i)\\ &= \partial\phi_r \delta r + \partial\phi_a \delta a + \phi(r_0,a_0,i)\end{aligned} \tag{7}$$

in which $\partial\phi(r_0,a_0,i)/\partial r = \partial\phi_r$ and $\partial\phi(r_0,a_0,i)/\partial a = \partial\phi_a$ are the phase derivatives along range and azimuth, and $\phi(r_0,a_0,i)$ is the phase of pixel (r_0,a_0). Inherently working on wrapped phase, we assume local phase varying no more than magnitude of $|\pi|$, and thus, Eq. 7 is reformulated into

$$\begin{aligned}\delta\phi(r,a,i) &= \langle \widehat{\phi}(r,a,i) - \widehat{\phi}(r_0,a_0,i)\rangle_{-\pi,\pi}\\ &= \partial\phi_r \delta r + \partial\phi_a \delta a\end{aligned} \tag{8}$$

$\nabla\phi(r_0,a_0,i) = (\partial\phi_r, \partial\phi_a)^T$ can be estimated using phase observations from neighboring pixels within a predefined square window.

The optimized LT-1 interferograms from Section 3.1 are used in Eq. 8, applying pixels from a 3×3 local window to estimate $\nabla\phi$ for each pixel. To account for varying phase quality among neighboring pixels, we adopt a weighted least-squares approach using the γ_{apt} map as weights, enhancing the accuracy of $\nabla\phi$ estimate. Additionally, to reduce artifacts from inherent phase wrapping in long-term accumulation and to facilitate subsequent time-series analysis, the original $N-1$ single-master interferograms are reformulated into $N-1$ consecutive pairs, $\phi_{k,k+1} = \phi_{k+1} - \phi_k$, where $k \in \mathscr{Z}_1$. The phase gradient, $\nabla\widehat{\phi}_{k,k+1} = \left[\partial\widehat{\phi}_r^{k,k+1}, \partial\widehat{\phi}_a^{k,k+1}\right]^T$, is then recursively estimated for all consecutive interferograms. For notational simplicity, we abbreviate $\nabla\widehat{\phi}_{k,k+1}$ as $\nabla\widehat{\phi}_k = \left[\partial\widehat{\phi}_r^k, \partial\widehat{\phi}_a^k\right]^T, k \in \mathscr{Z}_1$. The process is illustrated in Fig. 2B, I.

During the estimation process described above, a relatively small local window is used than a larger one, as the optimized phase already ensures noise suppression without the need to incorporate additional observations at cost of spatial resolution. Moreover, the spatial variation of atmospheric component at such scale is minor (Shi et al., 2022a). After spatial differentiation within the window, the residual atmospheric contribution becomes almost negligible in $\nabla\widehat{\phi}$. The same applies to residual orbital errors. At this stage, the primary contributors to the phase gradient are ground motion, height errors, and decorrelation effects. The approach for further identifying pixels susceptible to landsliding is presented in the next section.

3.2.2. Landslide points detection and clustering

The inherently localized decorrelation effects caused by various ground disturbances are intangible in phase gradient, as a result of introducing prominent spatial variability that blurs the boundaries of deformation zone, making landslide unidentifiable. The existing studies generally avoid using gradient-based methods in forested or highly vegetated areas (Cao et al., 2023; Zhang et al., 2024). In this study, we leverage the specific kinematic characteristic of landslide in Hong Kong, along with external meteorological data, to pre-locate landslide-susceptible pixels for the hazard early-warning.

As detailed in a rainfall-landslide correlation study by Brand et al. (1984), due to the widespread presence of colluvium on hillsides in Hong Kong, most slope collapses are tightly linked to short-duration, intensive rainfall events. The timing of these collapses often closely follows the hourly peaks of extreme rainstorms, revealing a slight lag between rainfall peaks and slope failures. A further study has also confirmed this hydromechanical characteristic of unstable hillslopes in Lantau Island (Dai et al., 1999). This rainfall-forcing mechanism implies that instantaneous hillslope slips triggered by extreme rainfall generate abrupt ground-motion signals, which are also captured in the corresponding phase gradient epochs of InSAR measurements. And the promptness of this deformation response enables direct correlation between the phase gradient, $\nabla\phi_k$, $k \in \mathscr{Z}_1$, and extreme rainfall data, provided that the time scales of the two datasets are aligned, allowing determination of whether a pixel is undergoing landsliding. Moreover, the correlation process helps identify and exclude disturbing pixels whose phase variations are dominated by factors such as soil moisture changes, vegetation dynamics, or height errors. Because extreme rainfall time series exhibit spike pattern with a consistent same sign across all temporal point, in clear contrast to the oscillating patterns typically

produced by these other phase components.

As illustrated in Fig. 1, major heavy rainfall events recorded across the five meteorological stations exhibit regional coherence and temporal synchrony, justifying the use of a General Extreme Rainfall Pattern (GERP) as a regional indicator of dominant hydrometeorological forcing for major slope movement. An exceptionally high rainfall amount was recorded at CCH on 2024-05-04, implying a localized rainfall anomaly. Its inclusion in the GERP computation diminish regional representativeness; instead, it enhances sensitivity to spatial heterogeneity, which potentially reduce the risk of overlooking landslides triggered by localized rainfall. Moreover, the broad distribution of colluvium on Lantau Island, which predisposes slopes to widespread collapses under extreme hydrometeorological forcing, further supports the use of GERP as a reasonable regional indicator (Dai et al., 1999; Wong et al., 1998).

In the study, hourly precipitation measurements, P, shown in Fig. 1, were used to compute the GERP, in which extreme events are defined as hourly records above the 99th percentile ($\widetilde{P}^{0.99}$) across all meteorological station (Lai et al., 2024). Specifically, if, at time t, the rainfall at meteorological station q exceeds this threshold, the extreme precipitation value is defined as $P_{q,t}^{ext} = P_{q,t}$ *if* $P_{q,t} > \widetilde{P}^{0.99}$. We suppose t_k denoting the time of k-th SAR scene. To make the rainfall data and $\nabla\phi$ comparable, the time scales of two data ought to get aligned. Extreme precipitation intensity $S_{q,k}^{ext}$ within SAR consecutive pair of k and $k+1$, is computed as summation of $P_{q,t}^{ext}$ within the corresponding time span: $S_{q,k}^{ext} = \sum_{t\in[t_k,t_{k+1}]} P_{q,t}^{ext}$. Then, the GERP is computed as arithmetic mean of the extreme precipitation data from the five stations, $S_k^{ext} = \frac{1}{5}\sum_{q=0}^{4} S_{q,k}^{ext}$.

In the landslide identification, as inherently varying decorrelation effects across pixels in optimized phase, we primarily employ γ_{apt} and a common threshold choice of 0.7 to mask out those unreliable pixels (Ferretti et al., 2011). Given a pixel at (r,a), we calculate its sample Pearson's correlation coefficient $\rho(r,a)$ between $\nabla\phi_k(r,a)$ and S_k^{ext} as follows:

$$\rho(r,a) = \frac{\sum_{k=0}^{N-2}\left(\nabla\widehat{\phi}_k - \Delta\overline{\phi}\right)\left(S_k^{ext} - \overline{S}^{ext}\right)}{\sqrt{\sum_{k=0}^{N-2}\left(\nabla\widehat{\phi}_k - \Delta\overline{\phi}\right)^2 \sum_{k=0}^{N-2}\left(S_k^{ext} - \overline{S}^{ext}\right)^2}} = \begin{bmatrix}\rho_0(r,a)\\ \rho_1(r,a)\end{bmatrix} \tag{9}$$

where $\nabla\overline{\phi}$ and $\overline{S}^{ext}$ denote the sample means of $\nabla\widehat{\phi}_k$ and $S_k^{ext}, k \in \mathscr{Z}_1$, respectively. The correlation coefficients between $[\partial\phi_r, \partial\phi_a]^T$ and the GERP is represented by vector $\rho = [\rho_0, \rho_1]^T$. Hereafter, by thresholding ρ, the pixels where $\Delta\phi$ shows temporal consistency with the GERP can be easily split out. That is, a pixel is regarded as landslide-prone, as long as either ρ_0 or ρ_1 exceeds a critical threshold. This critical threshold is tuned between 0.5 and 0.9, and the resulting variation in the number of retained pixels is examined to determine a reasonable cutoff value. Fig. 4 shows the curve of pixel count versus correlation threshold. After the threshold exceeds 0.75, the rate of change in pixel number decreases sharply and stables, indicating that 0.75 is an appropriate elbow point for thresholding ρ.

Landslide deformation exhibits spatial continuity. When the resolution of InSAR pixels is sufficient to resolve a sliding slope, deformation pixels should appear as spatially connected clusters. Thus, genuine landslide points identified through phase gradient analysis are expected to form dense local aggregations as well. Applying this constraint can improve the reliability of the detection results. In this study, descending and ascending SAR datasets were merged for subsequent cluster analysis, and cluster extraction was performed via GIS-based heatmap analysis, producing the final landslide map. The implementation procedures are overviewed in Fig. 2B, II.

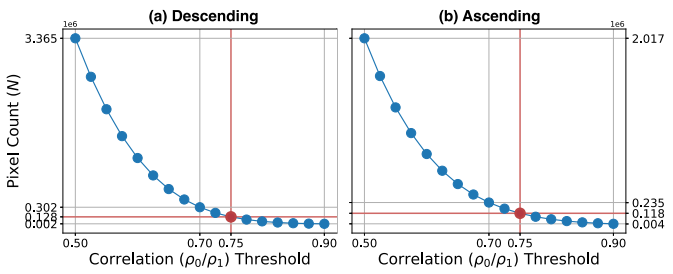

Fig. 4. Relationship curves between correlation threshold and pixel counts for (a) descending and (b) ascending results, given $\gamma_{apt} \geq 0.7$.

4. Results

4.1. Phase optimization from HARMIE

4.1.1. Simulated data

In Section 3.1.1, we illustrated how partially heterogeneous phase or amplitude pixels included in an i.i.d. pixel set bias $\widehat{\Gamma}$. To further test this, we simulated two 32-image stacks (700 × 700 pixels each) of speckle-free phase and amplitude data. The phase simulation of images 4, 14, and 30 are shown in Fig. 5 (1st column). A Gaussian elliptical phase was assigned as the deformation signal with a rate of 1.3 cm/year, modeled to vary exponentially and fluctuate with a magnitude of 0.5 cm. DEM error phases were added in regular, geometric shapes. To enhance phase variability, each of the four larger phase rectangles is split by a phase discontinuity line into two adjacent blocks with divergent values. Amplitude images followed a similar layout but with densely spaced contrasting rectangles in deformation zone to emphasize heterogeneity, as displayed in Fig. 5. Finally, a SLC speckle image stack of the same size was generated based on a fixed coherence matrix to couple the phase and amplitude images. And full simulation settings are provided in Section S1.4 in the supplementary material.

Upon homogeneous pixel sets Ω_{AP} of the simulated SLC stack were obtained, we need to find an optimal weight $D_0^{(0)}$ for the reference pixel p_0, for estimating $\widehat{\Sigma}$. Let the minimum weight as $D_{0,min} = \min\left\{D_0^{(l)}\right\}_{l\in\Omega_{AP}}$, and constrain $0 < D_0^{(0)} \leq D_{0,min}$. A scale parameter $\lambda \in [0.1, 1]$ can be introduced to scale the weight $D_0^{(0)} = \lambda D_{0,min}$. The problem turns to finding an optimal λ that minimize $\widehat{\Gamma}$ bias. Tuning λ from 0.1 to 1, we evaluate the Frobenius norm of coherence matrix bias, $\|\widehat{\Gamma} - \widetilde{\Gamma}\|_F$. Here, $\widetilde{\Gamma}$ denotes the large-sample approximation of the true coherence matrix Γ. As shown in the lower left panel of Fig. 5, $\|\widehat{\Gamma} - \widetilde{\Gamma}\|_F$ decreases and approaches convergence as λ approaches to 1. Therefore, $D_0^{(0)} = D_{0,min}$ is adopted for the estimation of $\widehat{\Gamma}$ in HARMIE.

To assess HARMIE's performance, we compared four methods—DespecKS (Ferretti et al., 2011), KUiper's Test on Phase Homogeneity (referred to as KUTPH) (Pepe et al., 2021), Quasi-Homogeneous Phase Selection (Q-HPS), and HARMIE for clustering homogeneous pixels within a 15 × 15 square window. Q-HPS follows the second stage of HARMIE but without the amplitude homogeneity constraint. Typical phase results from the four approaches shown in Fig. 5a-c, with corresponding homogeneous pixel numbers in Fig. 5d. Further evaluation was conducted across four spatially heterogeneous sub-regions (Fig. 6a–d).

Overall, the phase estimates resulting from the four approaches generally reflect the original phase pattern (Fig. 5). When focusing on the discontinuous boundaries as shown in zoomed-in regions of Fig. 6, noticeable blurring artifacts, however, appear in the results of DespecKS and KUPTH. Specifically, relying solely on amplitude homogeneity for pixel selection inadvertently imprints amplitude-pattern traces into phase estimation results (see the first row of Fig. 6a). This also leads to oversmoothing across intra-rectangle phase discontinuities, creating the ambiguities in sharp phase boundaries. In the case of KUTPH, although phase information is utilized during processing, the estimated phases exhibit an "ink-dripping" appearance along phase boundaries. This is indicative of struggling with handling local phase inconsistencies, which is further discussed in Section S1.4. In contrast, both the Q-HPS and

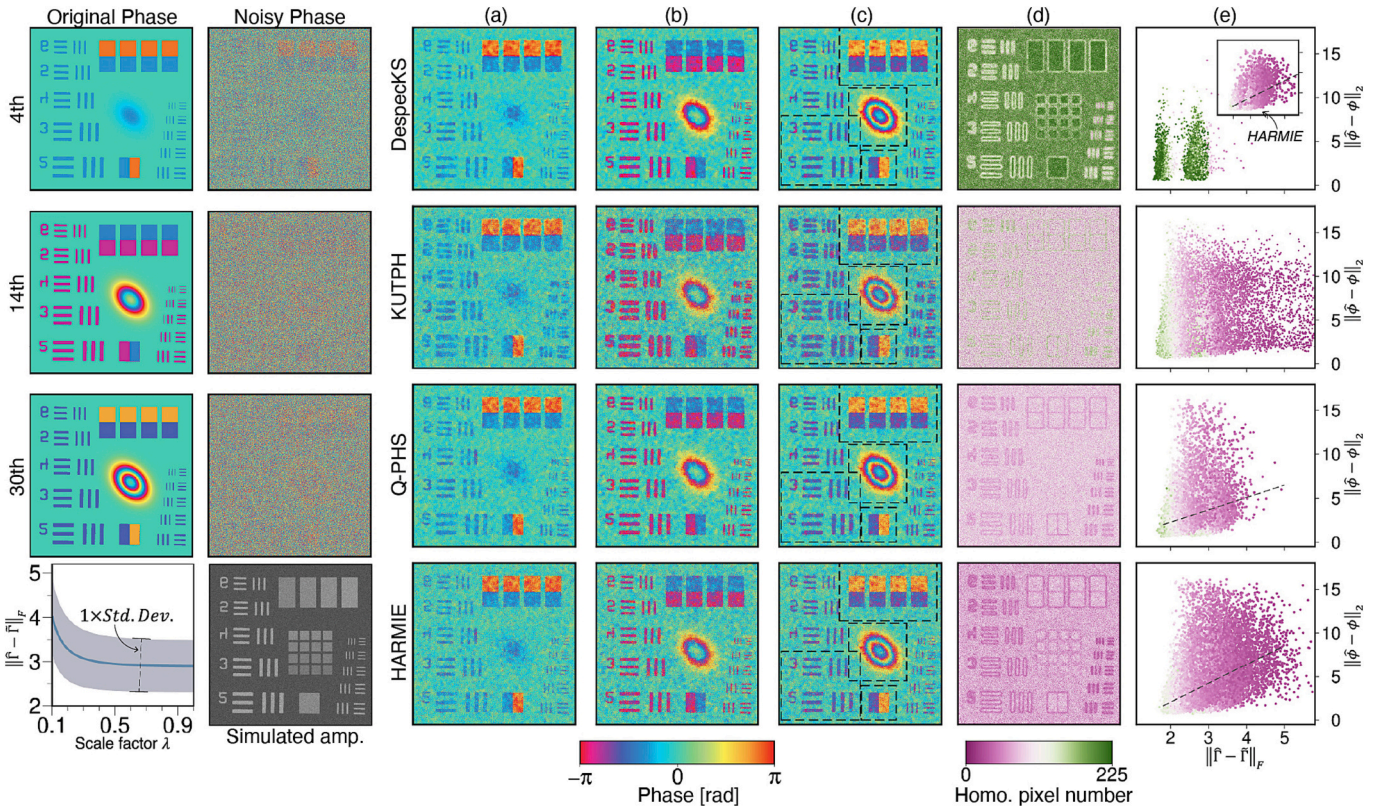

Fig. 5. Simulation components and phase estimation results across different approaches. The first two columns show the simulated noise-free and noisy phase maps for three representative acquisitions, while the bottom panels presents: (1) the convergence curve of the mean coherence matrix bias $\|\widehat{\Gamma}-\widetilde{\Gamma}\|_F$, obtained by adjusting the weight of reference p_0 via a scale factor λ with $D_0^{(0)}=\lambda D_{0,min}$ (the gray shaded area indicates one standard deviation across all pixels); (2) the simulated amplitude map. (a–c) Estimated phase maps resulting from DespecKS, Kuiper's Test on Phase Homogeneity (KUTPH), Quasi-homogeneous Phase Pixel Selection (Q-HPS), and HARMIE for the 4th, 14th, and 30th scenes. Dashed black boxes in (c) indicate zoomed-in areas shown in Fig. 6. (d) The homogeneous pixel map obtained by per method. (e) Scatter plots of $\|\widehat{\Gamma}-\widetilde{\Gamma}\|_F$ versus phase error $\|\widehat{\phi}-\phi\|_2$. The first row shows results in phase-heterogeneous zones for DespecKS and HARMIE in the inset, while the other plots illustrate results in amplitude-heterogeneous areas for KUTPH, Q-HPS, and HARMIE.

HARMIE approaches not only suppress interferometric speckle effectively but also reconstruct interferometric fringes and highlight sharp phase discontinuities more accurately. This demonstrates their advantages in handling local phase variability. The number of homogeneous pixels achieved by each method, as shown in Fig. 5d, also reflects their differing capacities to manage phase and amplitude heterogeneity.

For a more quantitative comparison for performance, we extracted buffered zones (7 pixels wide) around phase/amplitude discontinuities (Fig. S2, a and b) to assess phase estimation performance using coherence bias $\|\widehat{\Gamma}-\widetilde{\Gamma}\|_F$ and the L2-norm of phase estimation error $\|\widehat{\phi}-\phi\|_2$. The relationship between these metrics is plotted in Fig. 5e, revealing distinct performance characteristics. The scatter plots corresponding to DespecKS and KUTPH show a weak or unclear dependence between the estimation errors of $\widehat{\Gamma}$ and $\widehat{\phi}$, with substantial uncertainty in phase estimation, even in cases where the bias of $\widehat{\Gamma}$ is relatively small. In contrast, results from both Q-HPS and HARMIE demonstrate a clear positive correlation, with lower uncertainty in $\widehat{\phi}$ as $\|\widehat{\Gamma}-\widetilde{\Gamma}\|_F$ decreases (see also the inset in the first row of Fig. 5e). Notably, the HARMIE approach exhibits a stronger positive correlation between $\widehat{\Gamma}$ and $\widehat{\phi}$ biases compared to Q-HPS. Fig. S3 illustrates the density distribution of the scatter points from Fig. 5e. The deviations of $\widehat{\Gamma}$ and $\widehat{\phi}$ derived from the HARMIE approach are more densely concentrated in low-bias region. For Q-HPS, the scatter density splits into two clusters, likely due to the influence of amplitude heterogeneity incorporated into the coherence estimation. These findings suggest that enforcing both amplitude and phase homogeneity enhances the theoretical dependence between the accuracy of coherence matrix estimation and phase reconstruction.

Our simulated experiments confirmed the adverse effects of spatial heterogeneities in phase and amplitude on the final phase estimation. Among the methods compared, Q-HPS shows superior ability in capturing spatially heterogeneous phase features, while HARMIE achieves the most accurate estimates of both $\widehat{\Gamma}$ and $\widehat{\phi}$, owing to its more stringent and reliable homogeneous pixel selection, albeit with fewer selected pixels. Moreover, HARMIE shows strong reliability and effectiveness in mitigating interferometric speckle and preserving phase heterogeneity.

4.1.2. L-band Lutan-1 data

Given the high spatial resolution of LT-1 SAR SLCs over Lantau Island—typically comprising approximately 10,000 pixels in both range and azimuth, with a resolution of 1.7 m and 1.5 m, respectively—computational efficiency is a critical consideration. Accordingly, a more efficient parametric form of the GLRT approach was employed to construct amplitude homogeneity pixel set Ω_A (Parizzi and Brcic, 2011; S. Samiei Esfahany, 2017). Following the procedures described in Section 3.1.2, the remaining steps of HARMIE method were then applied to generate phase-optimized products from the noisy LT-1 interferograms. To access the performance of HERMIE in a real-world scenario, an alternative optimization result was generated using the Ω_A pixel set as a comparative baseline.

The optimized LT-1 interferograms of the descending pair (20230705–20240719) and the ascending pair (20230802–20240828) are presented in Fig. 7a and e, respectively. The corresponding γ_{apt} maps obtained from the different approaches are illustrated in Fig. S6 and discussed accordingly in the supplementary material. Selected zoom-in

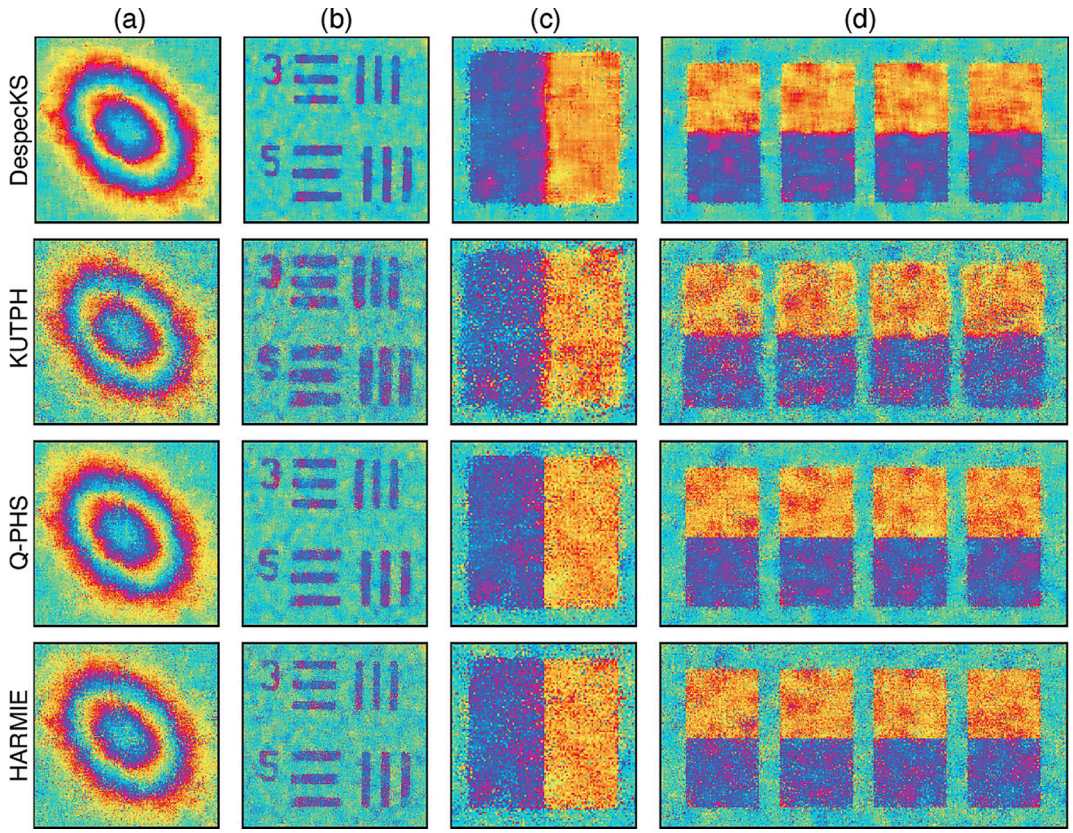

Fig. 6. Zoomed-in comparisons of the estimated phases with emphasis on the performance of recovering phase heterogeneity. (a-d) subregions outlined by dashed rectangles in Fig. 5.

views of the optimized interferometric phases are shown in Fig. 7b-d and f-h, where columns I and II correspond to results obtained based on the amplitude homogeneity (Ω_A) and the HARMIE ($\Omega_{AP} + W$) approaches, respectively. As stated in Section 2.3, landslide boundaries delineated from the two optical imageries are used as a reference for evaluating phase heterogeneity retrieval and are overlaid on the geocoded interferograms. Confirmed landslide extents are marked by solid black lines, while dashed black lines indicate zones of ongoing hillside movement identified from InSAR deformation results (detailed in Section 5 and shown in Fig. 10).

As seen in Fig. 7, the HARMIE-optimized phases exhibit greater magnitudes and clearer contrast with the background, with improved alignment to actual landslide extents, compared to the spatially smoother phases from the amplitude-based optimization. Despite the foreshortening effect evident in the ascending track (Fig. 7f), the HARMIE approach effectively preserves local phase variations over the collapsed slope. Moreover, the HARMIE-derived phases capture localized phase heterogeneity more accurately, as illustrated in Fig. 7c, g, and h.

A quantitative evaluation of phase heterogeneity retrieval was performed for several representative landslides in Fig. 7. For each landslide, the L_1-norm distance ω of the circular phase difference was calculated between the pixel phases within the landslide extent and the mean phase of the surrounding non-landslide background, providing a measure of heterogeneous phase magnitude. To compare amplitude-based and HARMIE results (ω_{amp} and ω_{HARMIE}), values were normalized by $\omega_{amp}+\omega_{HARMIE}$ for each landslide. As summarized in Table 1, ω_{HARMIE} is on average 13 % higher than ω_{amp} for the selected landslides. Nevertheless, it should be noted that the two-tier selection of HARMIE results in fewer pixels, which may retain decorrelated anomalies and slightly overestimate the previous quantitative evaluation, though the overall improvement remains. In severely decorrelated pixels with uniform-distributed phases, HARMIE may fail in pixel selection, leaving retrieved phase largely dominated by original spatial randomness.

Overall, under coherent conditions, these findings demonstrate superior capability of HARMIE to preserve fine-scale phase variations and magnitudes, thereby improving detection of both subtle ground movements and complete landslide extents compared to amplitude-homogeneity-based optimization.

4.2. Landslide mapping under forests

4.2.1. Landslide point detection results

The partial derivatives $\left[\partial\phi_r^k, \partial\phi_a^k\right]^T$ of ϕ_k for descending and ascending tracks were computed separately, following procedures in Section 3.2.1. With reference to the epochs of consecutive SAR acquisitions of $[t_k, t_{k+1}]$, the GERPs S_{desc}^{ext} and S_{asc}^{ext} of the two tracks were derived (time series in Fig. 8A1 and A2) for the subsequent correlation analysis. Both indices peaked at 118 mm in the third acquisition pair—20230915–20231013 and 20230927–20231122, coinciding with the occurrence epoch of Typhoon Koinu, during which substantial downslope movements were expected across unstable hillslopes on Lantau Island. To capture this response, phase gradient maps $\nabla\phi_2^{desc}$ and $\nabla\phi_2^{asc}$ from the third acquisition pair were generated, and four representative landslide regions are enlarged, all shown in Fig. 8A. Within these regions, feature points GP1–GP4 were selected, and their $\partial\phi_r$ and $\partial\phi_a$ time series are then plotted in Fig. 8A, marked by dark and light circles, respectively. For clarity, horizontal axes for plotting both $\nabla\phi_k$ and S_k^{ext} are anchored at the midpoint between t_k and t_{k+1}.

In Fig. 8A1 and A2, the $[\partial\phi_r, \partial\phi_a]^T$ time series for GP1-GP4 present a near-synchronous evolution with S_{desc}^{ext} or S_{asc}^{ext}. All major gradient spikes during the third epoch coincide with the peak of S^{ext} associated with the extreme rainfall event on October 9, 2023, brought by Typhoon Koinu.

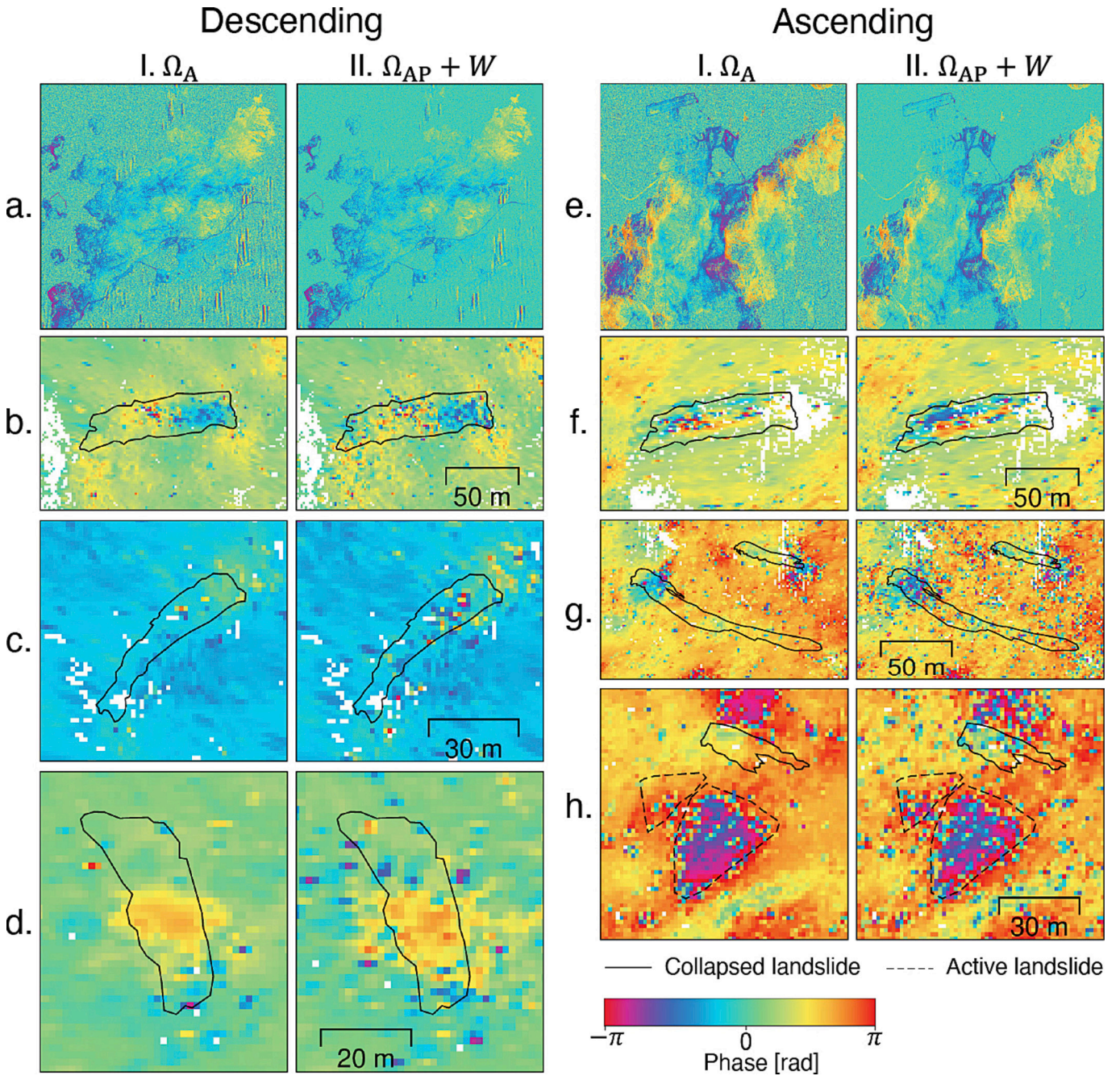

Fig. 7. Comparison of optimized descending and ascending LT-1 interferograms using the GLRT method (Ω_A) and HARMIE (Ω_{AP} and W). (a, e) show overviews of the optimized interferograms from both methods. (b–d, f–h) provide zoomed-in views highlighting local phase estimation details. The regions delineated by solid black lines represent hillslopes that have already collapsed (identified from TDOP), while those marked by dashed black lines indicate actively sliding hillslopes roughly delineated by our InSAR results (see Fig. 10 and Fig. 12).

Table 1
L_1-norm metric (ω) for phase heterogeneity in chosen landslides, over amplitude-based (ω_{amp}) and HARMIE (ω_{HARMIE}) retrieval methods, each normalized by $\omega_{amp} + \omega_{HARMIE}$. The view identifiers b-d and f-h correspond to the landslides depicted in Fig. 7.

Views	DESC		Views	ASC	
	ω_{amp}	ω_{HARME}		ω_{amp}	ω_{HARME}
b	0.4511	0.5489	f	0.4150	0.5850
c	0.4055	0.5945	g	0.4731	0.5268
d	0.4359	0.5641	h	0.4276	0.5724

This temporal alignment reinforces the earlier statements that extreme rainfall can trigger instantaneous landslide movements on unstable hillslopes. Spatially, $\nabla\phi_2^{desc}$ and $\nabla\phi_2^{asc}$ at the four landslide sites display markedly higher magnitude than surrounding values, closely matching the slope failure enclosures.

Across broader perspective in the study area, shown in Fig. 8A, numerous patchy noise artifacts are visible in the gradient results, largely due to severe signal decorrelation from ground disturbances, which obscure true landslide signals. By correlating $\nabla\phi$ and S^{ext}, landslide points can be distinguished from the ones disturbed by the artifacts. After applying density-based clustering, a comprehensive landslide point inventory was obtained. Fig. 8B presents the resulting landslide

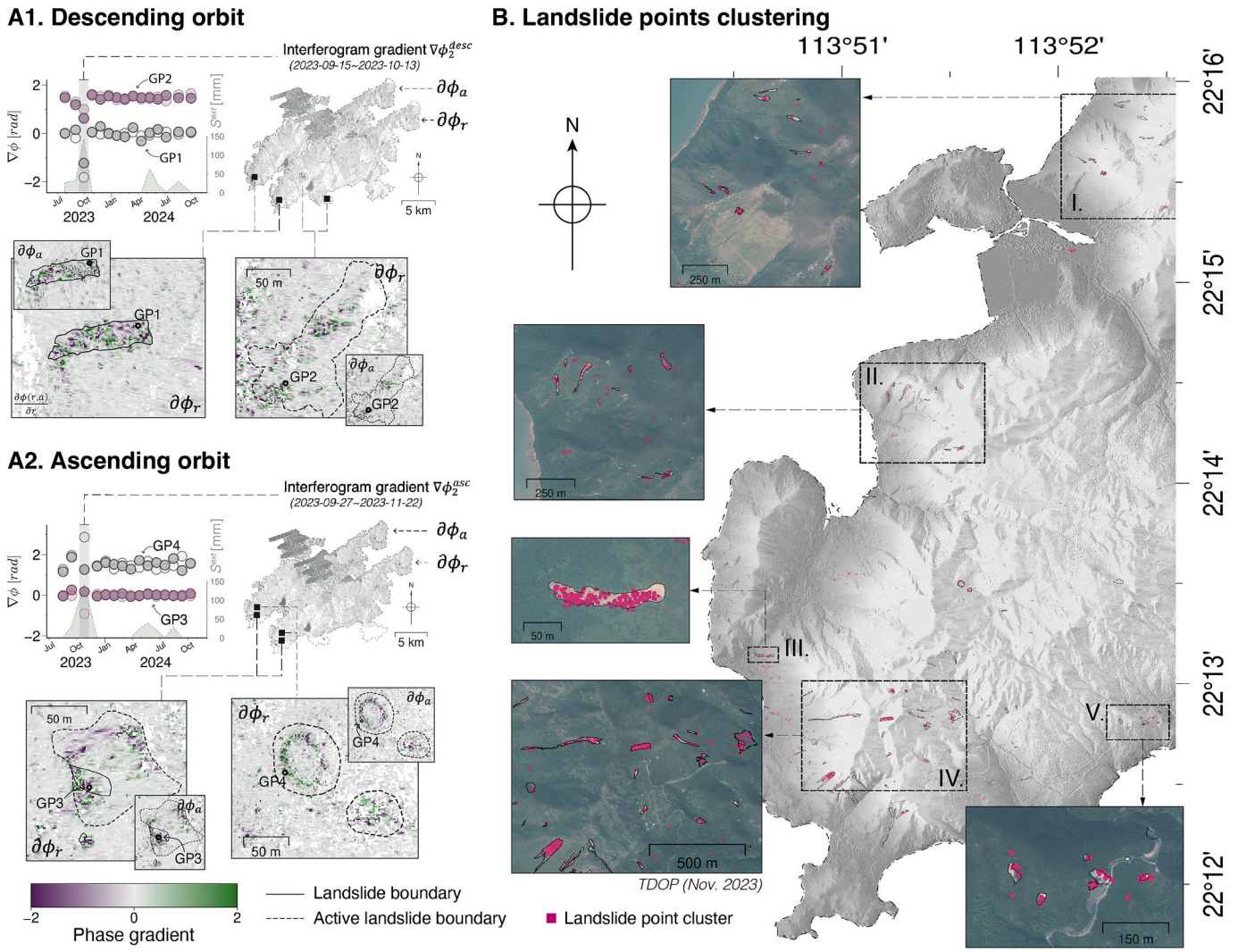

Fig. 8. Landslide detection process and results based on the descending and ascending optimized LT-1 interferograms. (A1–2) show the correlation analysis between phase gradients $\nabla\phi = [\partial\phi_r, \partial\phi_a]^T$ from the two tracks and the GERP S^{ext} to identify landslide points. Several typical regions with prominent gradients (involving the extreme rainfall event on October 9, 2023) are highlighted, and gradient time series of representative points GP1–GP4 are compared against GERP. (B) presents the clustered landslide points derived by integrating descending and ascending track results (illustrated for the landslide-prone western Lantau Island). Magenta squares indicate the final landslide point locations. Zoomed-in subregions overlaid on TDOP optical imagery are shown in (B, I-V). Solid and dashed black lines denote previously failed and actively sliding slopes, respectively. (For interpretation of the references to colour in this figure legend, the reader is referred to the web version of this article.)

distribution over western Lantau Island (major landslide-affected areas), superimposed on a hillshade image derived from the LiDAR DSM together with the hillslope failure boundaries determined in Section 2.3. The detected landslide clusters (magenta squares) align well with the TDOP-derived failure boundaries mapped in November 2023, confirming the reliability of the detection. This spatial match, together with the temporal agreement between the October 2023 peak in S^{ext} and corresponding $\nabla\phi$ spikes, indicates that these slope failures were triggered by the October extreme rainfall.

4.2.2. Comparison and evaluation of detection results

To evaluate the capability of HARMIE in preserving small-scale signals and its performance in landslide detection, an additional detection set was produced using amplitude-homogeneity-optimized LT-1 interferograms for comparison. The locations of 89 previously confirmed hillslope failures served as reference points to assess detection rates for both the HARMIE and amplitude approaches.

Detected and missed landslides for each method, as well as those identified by both, are shown in Fig. 9, with a statistical summary provided in Table 2 and full details in Table S5. The HARMIE approach successfully detected 72 landslides (80.9 % detection rate), including 26 missed by the amplitude approach. In contrast, the amplitude approach detected 48 landslides (53.9 % detection rate), with only two missed by HARMIE. A McNemar test performed on the structured results in Table 2 confirmed that HARMIE achieves a statistically significant improvement in detection rate over the amplitude method.

As illustrated in Fig. 9, although some landslides are recognized by the amplitude-based results, the detected points are generally sparser and less consistent with the actual outlines of the slope failures compared to HARMIE. Notably, HARMIE was able to detect even small failures with widths under 10 m. Furthermore, on-site landslide inventory data (slope failures from October 2023) were used to validate the results (marked by blue circles in Fig. 9b, d, h, and i). To be noted, complementary on-site inspections were generally conducted along

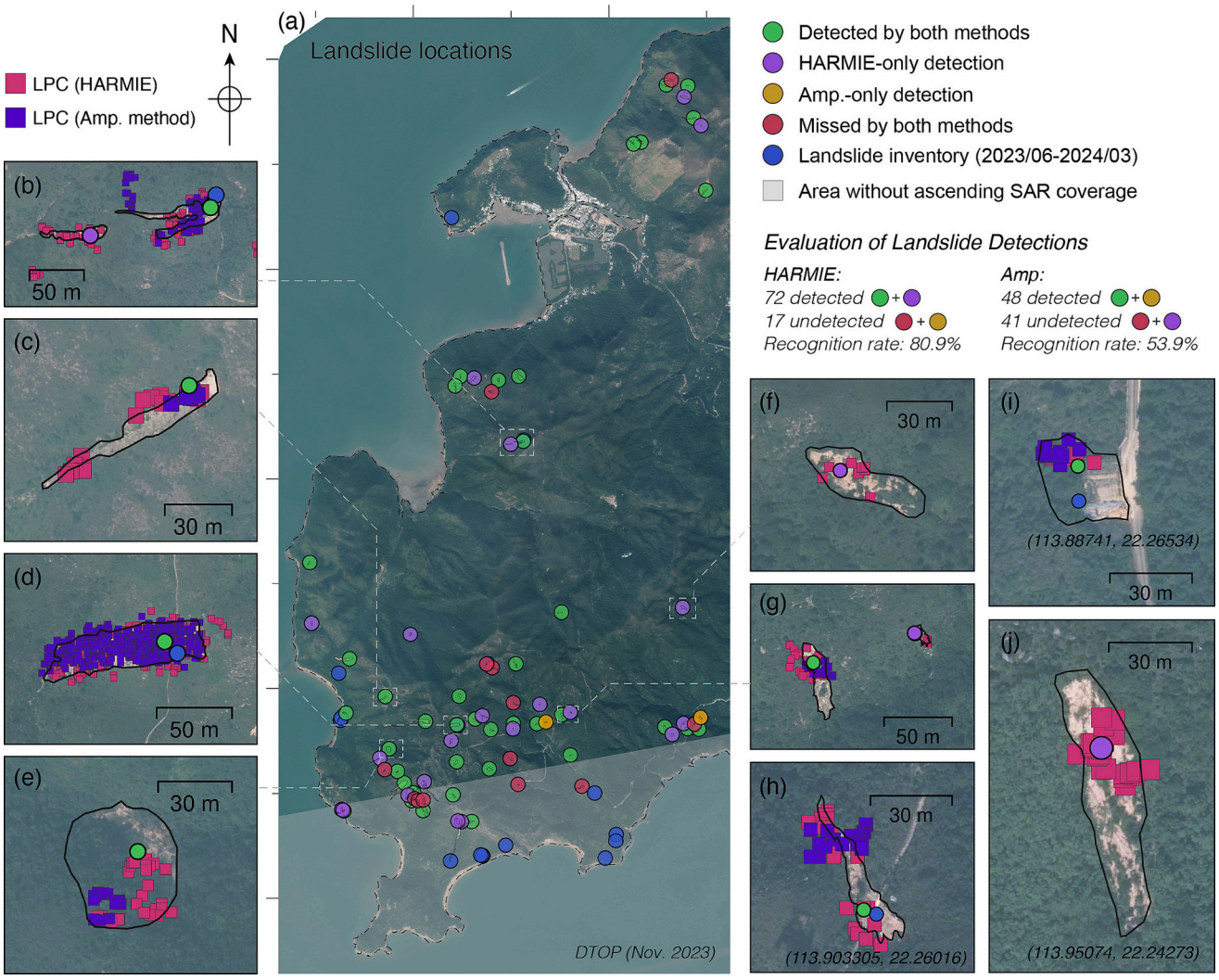

Fig. 9. Comparison of landslide detection results using the amplitude-homogeneity method (blue/purple squares) and the proposed HARMIE method (magenta squares). (a) Overview of landslide locations: green = detected by both, purple = HARMIE-only detection, yellow = amplitude-homogeneity-only detection, red = missed by both, and blue = field inventory. Light-gray shading marks areas without ascending SAR coverage. (b–j) Examples of localized clusters showing detection distributions. Overall, HARMIE achieved a 27 % higher recognition rate (80.9 %) than the amplitude method (53.9 %), detecting 72 versus 48 landslides. (For interpretation of the references to colour in this figure legend, the reader is referred to the web version of this article.)

Table 2

Statistical comparison of landslide detections between the HARMIE and amplitude-based approaches. The McNemar test statistic, $\chi^2 = (|b-c|-1)^2/(b+c) = 529/28 > \chi^2_{0.05,1} = 3.84$, indicates that the HARMIE approach achieves a statistically significant improvement in detection rate over the amplitude method.

		Amplitude method		
		Detected	Undetected	Total
HARMIE	Detected	46	26	72
	Undetected	2	15	17
	Total	48	41	89
McNemar test statistic χ^2	χ^2=529/28>$\chi^2_{0.05,1}$=3.84			

accessible roads or hiking trails, which led to genuine remote and steep mountain where no prior inventory records existed. Certain failures in southern Lantau recorded during field inspections were not detected in the InSAR results, as they lay outside the ascending LT-1 coverage and were less sensitive in the descending track view; several undetected landslides marked by red circles also fall within this area. Overall, when integrated with the proposed landslide detection method, HARMIE demonstrated enhanced preservation of localized hillslope displacement signal and achieved a 27 % higher detection rate than the amplitude-homogeneity-based approach, confirming the effectiveness of the proposed landslide identification framework.

5. Discussion

5.1. Characterizing hidden active slopes

In contrast to the already-collapsed hillslopes, hidden active hillslopes, whose sliding signatures are present but often visually obscured beneath canopy, may pose a greater potential risk during future extreme rainfall events, warranting heightened attention in natural hazard

management and early warning. The detection result reports landslide points clustering frequently outside of visible displacement ruptures, suggesting possible ongoing downslope movement. In this study, InSAR deformation time series are used to characterize these hidden active slopes and substantiate their identification.

In InSAR time series processing, HARMIE-optimized interferograms were configured in a 4-sequential interferometric network, retaining pixels with $\gamma_{apt} > 0.5$ for phase unwrapping (Costantini, 1998), and deriving deformation time series using MintPy (Mirzaee et al., 2023; Zhang et al., 2019). The final ascending scene from 20241023 was excluded due to the absence of precise orbit data. Using the LiDAR-derived DSM, two terrain sensitivity index maps corresponding to descending and ascending LT-1 SAR geometries were generated to project LOS deformations into the downslope direction, with pixels having index values below 0.2 masked out (Van Natijne et al., 2022).

From the detected landslide point clusters and their corresponding downslope spatiotemporal deformations, ten active landsliding hillslopes (ALHs) were identified, and their approximate movement extents were delineated from the spatial distribution of deformation rates. For each extent, the mean slope, aspect, elevation, and downslope InSAR velocity were calculated, and these attributes, together with the location coordinates, are summarized for ALHs ID 0–9 in Table 3. The representative ALH0–5, along with their InSAR-derived downslope displacements, are shown in Fig. 10 and Fig. 12 for detailed analysis in the following sections, with the remaining minor ALHs presented in Fig. S8. As shown in Table 3, most active hillslope instabilities occur on slopes steeper than 20° at moderate to high elevations, though the affected areas vary substantially, ranging from several hundred to over 10,000 m^2. In addition, the predominantly southeast- and southwest-facing aspects of these unstable hillslopes correspond to windward orientations under the prevailing summer monsoon, making them more directly exposed to intense monsoon rainstorms (Dai and Lee, 2002). Combined with prolonged solar radiation on these aspects, this exposure likely amplifies soil moisture fluctuations, accelerates weathering, and consequently increases landslide susceptibility (Li et al., 2023). One notable exception is ALH4, which, despite a moderate slope of 16.4°, an aspect of 69.7 and a relatively low elevation of 49.2 m, spans a considerable area of 12,142 m^2; its characteristics will be discussed in detail with reference to geological materials in the following section.

5.2. Slope kinematics under extreme rainfall

For the representative ALH0–4, Fig. 10 presents the spatial distribution of detected landslide points (1st column), 3D visualizations of the corresponding InSAR-derived downslope deformation rates from the viewing angle indicated by the dashed arrow (2nd column), and the downslope deformation time series of feature points P1-P5 selected for each landslide (Fig. 10d). Average hourly and monthly rainfall data from meteorological stations on Lantau Island are plotted alongside the deformation time series, with the horizontal dashed line marking the 99th-percentile hourly rainfall threshold as an indicator of extreme precipitation. This integrated visualization enables a comprehensive characterization of the landslide kinematics.

The InSAR deformation rates reveal distinct downslope movements on these hillsides. Within the deforming regions (enclosed by dashed circles), the dense clustering of detected landslide points indicates slope motion patterns dominated by hydrometeorological forcing under extreme rainfall. The downslope deformation time series, analyzed alongside rainfall records, reconstruct this hydrometeorological response. As shown in Fig. 10d, these unstable areas remained largely immobile during the early rainfall phase of July–September 2023, until the subsequent extreme precipitation of October 2023 triggered abrupt accelerations of downslope slipping. A second acceleration occurred mainly during July–September 2024 under prolonged rainfall with two relatively moderate rainstorms, particularly for P1–P3. In contrast, the extreme rainstorm of May 2024 did not produce the expected abrupt downslope displacement in the time series. We found that both major acceleration events in 2023 and 2024 were preceded by prolonged antecedent rainfall, unlike the sudden and isolated event in May 2024. This suggests that sustained antecedent rainfall likely maintained elevated soil moisture levels, reducing shear strength (Lu and Godt, 2013) and preconditioning the slopes for shear sliding under subsequent intense rainfall.

The ALH4, as noted earlier, is an exceptional case located near the coastline at low elevation with a relatively gentle slope compared to other active sites. P5 time-series deformation in Fig. 10d suggests that the extreme rainfall from Typhoon Koinu in October 2023 initiated the slope's destabilization process. An abrupt displacement was detected in January 2024 without concurrent hydrological triggers. Subsequent Google Earth imagery from 14 February 2024 (Fig. 10 c1) morphological features consistent with slope failure. Geological data (Fig. 11) indicate that the landslide area coincides with the intersection of an observed fault and is surrounded by Quaternary alluvial and debris flow deposits. The combination of loose sediments and fault-related weakening likely predisposed the slope to failure.

5.3. The critical combination: How antecedent and extreme rainfall jointly trigger landslides

As noted by Brand et al. (1984), antecedent rainfall without high-intensity events may contribute to minor landslides in Hong Kong. In this process, early rainfall infiltration raises initial soil moisture, and subsequent prolonged rainfall further predisposes slopes to destabilization (Lu and Godt, 2013). To investigate such landslide, we used average rainfall between t_k and t_{k+1} to represent sustained precipitation intensity and examined its correlation with the phase gradient series $\nabla\phi$

Table 3
Identified Active Landsliding Hillslopes (ALH) 0–10 through the proposed framework. The slope (°), aspect (°), height (m), and InSAR downslope velocity (cm/year) are mean values computed cross the pixels within the delineated ALH extent. The asterisk (*) indicates landslides that has collapsed within InSAR monitoring period but not induced by the typhoon events in 2023, and the dagger (†) denotes the landslides that are (also) driven by antecedent rainfall (see discussion in Section 5.3).

ID	Coordinate (°)		Slope (°)	Aspect (°)	Height (m)	Approximate landslide area (m^2)	InSAR downslope velocity (cm/year)
	Longitude	Latitude					
0	113.85650	22.21308	30.2	140.6	295.3	1282	6.4
1	113.85876	22.21404	20.2	121.0	225.8	6871	8.2
2	113.85920	22.22498	25.6	85.9	319.6	2532	5.9
3	113.85984	22.22444	24.3	123.3	297.3	1015	4.5
4*	113.92312	22.21584	16.4	236.1	49.2	12,142	5.2
5*, †	113.89616	22.26434	31.7	260.1	187.4	9352	2.4
6	113.85498	22.21604	29.0	96.4	363.4	411	2.1
7	113.87319	22.21328	32.3	137.0	126.3	262	4.2
8	113.87016	22.25908	29.2	246.1	182.2	988	1.7
9	113.89116	22.27043	30.5	266.1	200.8	647	1.2
10†	113.87136	22.22513	12.8	69.7	419.2	2389	2.9

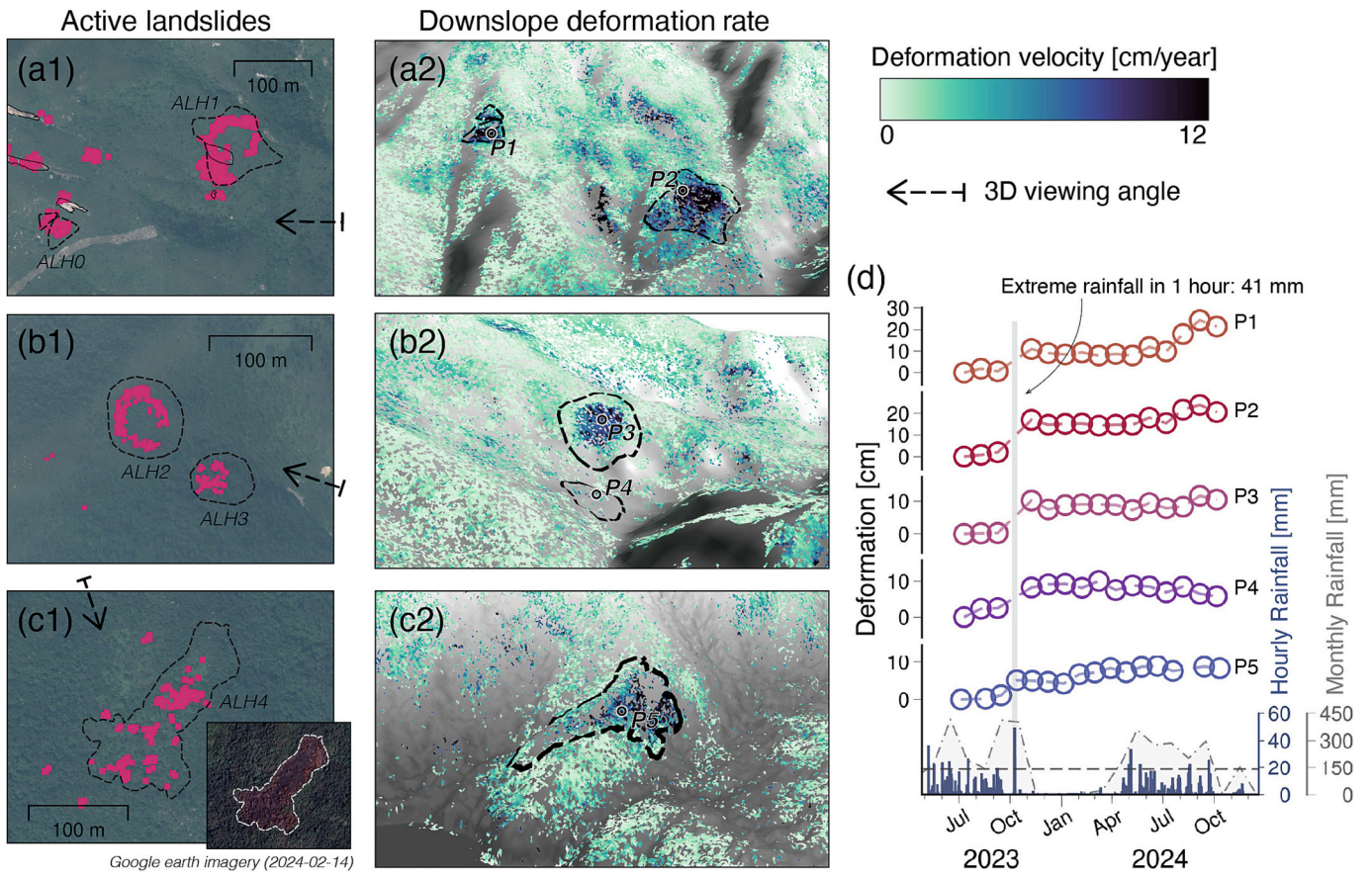

Fig. 10. ALH0–4 and corresponding InSAR results projected along the downslope direction. (a–c1) show identified landslide point clusters superimposed on the TDOP. To be noted, Google Earth imagery captured on February 14, 2024, confirms visible scarp in ALH4, verifying a recent slope failure and prompting an update to the landslide boundary. (a–c2) display 3D visualizations of InSAR displacements projected downslope, overlaid on the LiDAR-derived DSM, viewed from the direction indicated by dashed arrows. Featured points P1–P5 are marked for reference. (d) plots their corresponding time series of InSAR downslope displacements alongside hourly and monthly rainfall data.

Fig. 11. 1:200,000 geological map of the ALH4 area. Its location intersects with at a fault and is surrounded by Quaternary alluvial and debris flow deposits.

for landslide identification. Using the method described in Section 3.2.2, newly detected clustered landslide points were identified and marked by white-filled red rectangles (LPC1), contrasting to GERP-derived clusters (LPC0). These clusters are interpreted as slopes destabilized under antecedent prolonged rainfall.

Among them, one new active landslide, ALH10, was identified, with its location, morphology, and movement attributes detailed in Table 3. In addition, ALH5, previously detected, also includes this type of landslide points, suggesting a possible dual motion mechanism that will be discussed later. The detection points and kinematics of the corresponding hillslopes are visualized in Fig. 12 in a same manner as Fig. 10, with representative points labeled at the toe (P7 and P9), mid-slope (P8, P11, and P12), and crest (P6 and P10) for deformation time series analysis per slope.

The time series overall reveal progressive downslope deformation in response to sustained rainfall, confirming hydrometeorological forcing by antecedent precipitation. During dry or hot period, opposite motion trends were observed, likely due to relatively stronger evapotranspiration against wetting effect and associated soil shrinkage (Li et al., 2023). Considering the spatial distribution of points, mid-slope acceleration occurred first during the September 2023 rainfall (e.g., P8 in ALH10; P11 and P12 in ALH5), whereas upslope acceleration didn't initiate until the extreme rainfall in the following month (P6 and P10). This pattern suggests the transient development of a saturation zone in the central slope, initiating sliding that subsequently propagated rearward toward the scarp.

Specifically for ALH5 (Fig. 12b), the landslide exhibited a combined response to both extreme and antecedent rainfall. Time series at P12 showed abrupt acceleration following the October 2023 rainstorm, while P9–P11 displayed progressive deformation linked to sustained rainfall. With account of the landslide's relatively large spatial extent, this temporal divergence between the alternating LPC0- and LPC1-type responses may indicate that different portions of the landslide body were activated in distinct manners, possibly reflecting multiple sliding blocks. Under significant acceleration from these joint hydrological effects,

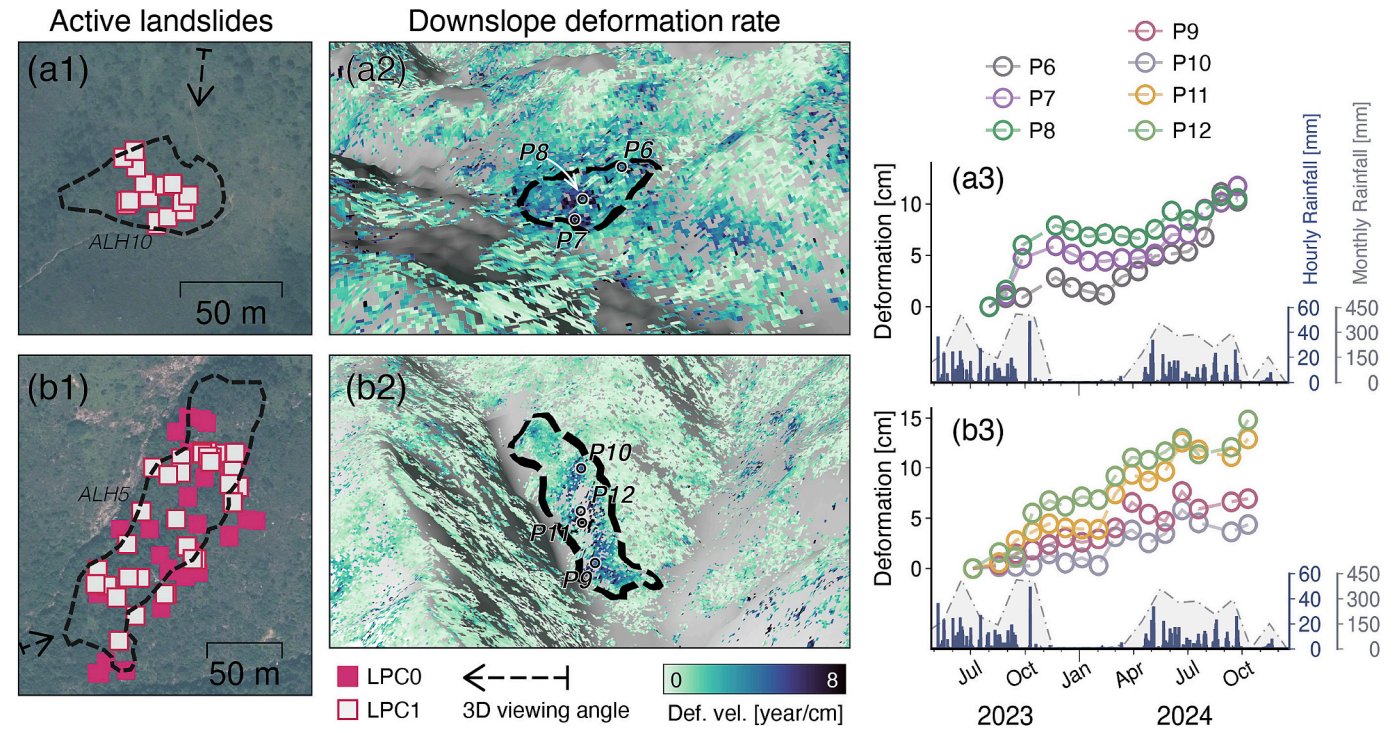

Fig. 12. ALH5 and ALH10 and corresponding downslope-projected InSAR displacements. (a–b1) show landslide point clusters (LPC0) identified via GERP analysis (magenta squares) superimposed on the TDOP. White-filled red squares indicate additional landslide points (LPC1) identified based on average rainfall pattern analysis. Dashed black arrows mark the viewing angles of the 3D downslope-projected InSAR deformation visualizations in (a–b2). Feature points at the toe (P7 and P9), mid-slope (P8, P11, and P12), and crest (P6 and P10) are selected, and their time series of downslope InSAR displacements are shown in (a–b3), compared against hourly and monthly rainfall data. (For interpretation of the references to colour in this figure legend, the reader is referred to the web version of this article.)

Google Earth imagery (27 August 2024) further confirms hillslope collapse, with visible scarps (Fig. S9), while deformation continued afterward. Overall, the case of ALH5 underscores the complexity and diversity of landslide initiation mechanisms in the study area, warranting more detailed investigations in future work.

6. Conclusion

This study addresses key limitations of InSAR in detecting small-scale landslides hidden beneath forest in Hong Kong's subtropical mountains. We developed a new framework with two methodological advances: 1) HARMIE, which optimize homogeneous pixels through joint amplitude-phase analysis and harmonizes inter-pixel phase imbalance; and 2) a phase gradient-based detection approach that links slope responses to extreme rainfall (GERP). Applied to Lantau Island, a hotspot of slope failures in Hong Kong, this framework enhanced the effectiveness of L-band InSAR for landslide mapping. The key findings are as follows:

(1) Improved detection performance. HARMIE outperformed conventional amplitude-based methods in both simulated and real datasets, accurately capturing localized phase variability. This critical capability enabled the widespread recognition of subtle landslides, as small as 10 m in width, achieving a 27 % higher detection rate of hillslope failures triggered by the October 2023 rainfall event compared to amplitude method.
(2) Active slope destabilization under extreme rainfall. We identified 10 active landslides hidden under dense vegetation. Time-series analysis revealed the shear slipping of slopes coinciding with short-duration, high-intensity rainfall, while in several cases, antecedent rainfall preconditioned slopes for subsequent accelerating destabilization.
(3) Antecedent rainfall as a secondary factor in rainfall-landslide interactions. Prolonged antecedent rainfall was found to drive seasonal progressive creep on minor hillslopes, while one site exhibited dual acceleration responding to both antecedent and extreme rainfall. These results highlight that, such sustained hydrological process, though a minor impact in the study area, potentially provide complementary insight into the complex mechanisms of hillslope failure.

This study represents one of the first attempts to locate small, forest-covered landslides using L-band InSAR. The findings confirm extreme rainfall as the dominant trigger while highlighting the secondary role of antecedent hydrological conditioning. Looking forward, greater emphasis should be placed on active landslide detection and translating technological advances into operational early-warning systems for Hong Kong and similar forested, mountainous region worldwide.

CRediT authorship contribution statement

Ziyuan Li: Writing – review & editing, Writing – original draft, Visualization, Validation, Software, Methodology. **Guoqiang Shi:** Writing – review & editing, Validation, Supervision, Resources, Methodology, Funding acquisition, Data curation, Conceptualization. **Songbo Wu:** Writing – review & editing, Validation, Software, Methodology, Data curation. **Tao Li:** Writing – review & editing, Data curation. **Zhong Lu:** Writing – review & editing, Validation, Methodology. **Xiaoli Ding:** Writing – review & editing, Supervision, Resources.

Declaration of competing interest

The authors declare that they have no known competing financial interests or personal relationships that could have appeared to influence the work reported in this paper.

Data availability

Data will be made available on request.

Acknowledgements

This work is supported in part by the National Natural Science Foundation of China (Grant No. 42304052, No. 42504044, & No.42330717), the Research Grants Council of Hong Kong (Grant No. 15229523, No. 25202125), the UGC-PolyU Grants (Grant No. P0050333, No. P0045896 & No. P0054628), and the Otto Poon Charitable Foundation (Grant No. P0055919). We thank the Land Satellite Remote Sensing Application Center, China, for providing LT-1 SAR imagery and precise orbit data. We are particularly grateful to Dr. Jingxin Hou for his valuable assistance with LT-1 SAR data processing. We also thank the Geotechnical Engineering Office (GEO) for the landslide inventory, the Civil Engineering and Development Department (CEDD) for the DSM, the Lands Department of the Hong Kong SAR for the TDOP data, and the Hong Kong Observatory for providing hourly precipitation data.

Appendix A. Supplementary data

Supplementary data to this article can be found online at https://doi.org/10.1016/j.rse.2025.115039.

References

Ansari, H., De Zan, F., Bamler, R., 2018. Efficient phase estimation for Interferogram stacks. IEEE Trans. Geosci. Remote Sensing 56, 4109–4125. https://doi.org/10.1109/TGRS.2018.2826045.

Brand, E.W., Premchitt, J., Phillipson, H.B., 1984. Relationship between rainfall and landslides in Hong Kong. In: Proceedings of the 4th International Symposium on Landslides, Toronto, 1984, pp. 276–284.

Cao, Y., Hamling, I., Massey, C., Upton, P., 2023. Slow-moving landslides triggered by the 2016 mw 7.8 Kaikōura earthquake, New Zealand: a new InSAR phase-gradient based time-series approach. Geophys. Res. Lett. 50. https://doi.org/10.1029/2022GL102064.

Chen, B., Li, Z., Song, C., Yu, C., Tomás, R., Du, J., Li, X., Mugabushaka, A., Zhu, W., Peng, J., 2025. Slip surface, volume and evolution of active landslide groups in Gongjue County, eastern Tibetan plateau from 15-year InSAR observations. Remote Sens. Environ. 324, 114763. https://doi.org/10.1016/j.rse.2025.114763.

Costantini, M., 1998. A novel phase unwrapping method based on network programming. IEEE Trans. Geosci. Remote Sensing 36, 813–821. https://doi.org/10.1109/36.673674.

Dai, F.C., Lee, C.F., 2002. Landslide characteristics and slope instability modeling using GIS, Lantau Island, Hong Kong. Geomorphology 42, 213–228. https://doi.org/10.1016/S0169-555X(01)00087-3.

Dai, F.C., Lee, C.F., Wang, S.J., 1999. Analysis of rainstorm-induced slide-debris flows on natural terrain of Lantau Island, Hong Kong. Eng. Geol. 51, 279–290. https://doi.org/10.1016/S0013-7952(98)00047-7.

Ferretti, A., Fumagalli, A., Novali, F., Prati, C., Rocca, F., Rucci, A., 2011. A new algorithm for processing interferometric data-stacks: SqueeSAR. IEEE Trans. Geosci. Remote Sens. 49, 3460–3470. https://doi.org/10.1109/TGRS.2011.2124465.

Goodman, N.R., 1963. Statistical analysis based on a certain multivariate complex Gaussian distribution (an introduction). Ann. Math. Statist. 34, 152–177. https://doi.org/10.1214/aoms/1177704250.

Guarnieri, A.M., Tebaldini, S., 2008. On the exploitation of target statistics for SAR interferometry applications. IEEE Trans. Geosci. Remote Sensing 46, 3436–3443. https://doi.org/10.1109/TGRS.2008.2001756.

Handwerger, A.L., Fielding, E.J., Huang, M.-H., Bennett, G.L., Liang, C., Schulz, W.H., 2019. Widespread initiation, reactivation, and acceleration of landslides in the northern California coast ranges due to extreme rainfall. J. Geophys. Res. Earth 124, 1782–1797. https://doi.org/10.1029/2019JF005035.

Hanssen, R.F., 2001. Radar Interferometry: Data Interpretation and Error Analysis. Springer Science & Business Media.

Hu, X., Bürgmann, R., Fielding, E.J., Lee, H., 2020. Internal kinematics of the Slumgullion landslide (USA) from high-resolution UAVSAR InSAR data. Remote Sens. Environ. 251, 112057. https://doi.org/10.1016/j.rse.2020.112057.

Jiang, M., Ding, X., Hanssen, R.F., Malhotra, R., Chang, L., 2015. Fast statistically homogeneous pixel selection for covariance matrix estimation for multitemporal InSAR. IEEE Trans. Geosci. Remote Sensing 53, 1213–1224. https://doi.org/10.1109/TGRS.2014.2336237.

Just, D., Bamler, R., 1994. Phase statistics of interferograms with applications to synthetic aperture radar. Appl. Optics 33, 4361. https://doi.org/10.1364/AO.33.004361.

Lai, Y., Li, J., Lee, T., Tse, W.-P., Chan, F.K.S., Chen, Y.D., Gu, X., 2024. A 131-year evidence of more extreme and higher total amount of hourly precipitation in Hong Kong. Environ. Res. Lett. 19, 034008. https://doi.org/10.1088/1748-9326/ad21b1.

Li, Z., Hu, J., Zhang, X., Zheng, W., Wu, W., Chen, Y., Tang, P., Gui, R., 2023. Characterization of elastoplastic behavior and retrieval of active zone depth for expansive soil slopes in the middle-route channel head of the south-to-north water diversion project, China, using InSAR time series. Remote Sens. Environ. 295, 113666. https://doi.org/10.1016/j.rse.2023.113666.

Lu, N., Godt, J.W., 2013. Hillslope Hydrology and Stability. Cambridge University Press, Cambridge.

Mardia, K.V., Jupp, P.E., 2000. Directional Statistics, Wiley Series in Probability and Statistics. J. Wiley, Chichester, New York.

Mirzaee, S., Amelung, F., Fattahi, H., 2023. Non-linear phase linking using joined distributed and persistent scatterers. Comput. Geosci. 171, 105291. https://doi.org/10.1016/j.cageo.2022.105291.

Parizzi, A., 2020. Potential of an automatic grounding zone characterization using wrapped InSAR phase. In: IGARSS 2020–2020 IEEE International Geoscience and Remote Sensing Symposium. Presented at the IGARSS 2020–2020 IEEE International Geoscience and Remote Sensing Symposium. IEEE, Waikoloa, HI, USA, pp. 802–805. https://doi.org/10.1109/IGARSS39084.2020.9323199.

Parizzi, A., Brcic, R., 2011. Adaptive InSAR stack multilooking exploiting amplitude statistics: a comparison between different techniques and practical results. IEEE Geosci. Remote Sensing Lett. 8, 441–445. https://doi.org/10.1109/LGRS.2010.2083631.

Pepe, A., Mastro, P., Jones, C.E., 2021. Adaptive multilooking of multitemporal differential SAR interferometric data stack using directional statistics. IEEE Trans. Geosci. Remote Sensing 59, 6706–6721. https://doi.org/10.1109/TGRS.2020.3030003.

Ross, N., Milillo, P., Dini, L., 2024. Automated grounding line delineation using deep learning and phase gradient-based approaches on COSMO-SkyMed DInSAR data. Remote Sens. Environ. 315, 114429. https://doi.org/10.1016/j.rse.2024.114429.

Samiei Esfahany, S., 2017. Exploitation of distributed scatterers in synthetic aperture radar interferometry. Delft Univ. Technol. https://doi.org/10.4233/UUID:22D46F1E-9061-46B0-9726-760C41404B6F.

Samiei-Esfahany, S., Hanssen, R., 2017. On the evaluation of second order phase statistics in SAR interferogram stacks. EOGE 1. https://doi.org/10.22059/eoge.2017.63865.1016.

Samiei-Esfahany, S., Martins, J.E., van Leijen, F., Hanssen, R.F., 2016. Phase estimation for distributed Scatterers in InSAR stacks using integer least squares estimation. IEEE Trans. Geosci. Remote Sens. 54, 5671–5687. https://doi.org/10.1109/TGRS.2016.2566604.

Shi, G., Huang, B., Leung, A.K., Ng, C.W.W., Wu, Z., Lin, H., 2022a. Millimeter slope ratcheting from multitemporal SAR interferometry with a correction of coastal tropospheric delay: a case study in Hong Kong. Remote Sens. Environ. 280, 113148. https://doi.org/10.1016/j.rse.2022.113148.

Shi, G., Huang, B., Ma, P., Lin, H., 2022b. Distributed scatterer interferometry for forested and hilly areas using a topographical homogeneous filtering. Remote Sens. Lett. 13, 460–469. https://doi.org/10.1080/2150704X.2022.2039414.

Touzi, R., Lopes, A., Bruniquel, J., Vachon, P.W., 1999. Coherence estimation for SAR imagery. IEEE Trans. Geosci. Remote Sensing 37, 135–149. https://doi.org/10.1109/36.739146.

Van Natijne, A.L., Bogaard, T.A., Van Leijen, F.J., Hanssen, R.F., Lindenbergh, R.C., 2022. World-wide InSAR sensitivity index for landslide deformation tracking. Int. J. Appl. Earth Observat. Geoinform. 111, 102829. https://doi.org/10.1016/j.jag.2022.102829.

Wong, H.N., Lam, K.C., Ho, K.K.S., 1998. Diagnostic report on the November 1993 natural terrain landslides on Lantau Island (no. GEO report no. 69), GEO report. In: Geotechnical Engineering Office, Civil Engineering Department, Government of the Hong Kong Special Administrative Region, Hong Kong.

Wu, S., Zhang, B., Ding, X., Shahzad, N., Zhang, L., Lu, Z., 2022. A hybrid method for MT-InSAR phase unwrapping for deformation monitoring in urban areas. Int. J. Appl. Earth Obs. Geoinf. 112, 102963. https://doi.org/10.1016/j.jag.2022.102963.

Yao, S., Balz, T., 2024. Phase-based similarly Decorrelated pixel selection and phase-linking in InSAR using circular statistics. IEEE Trans. Geosci. Remote Sensing 62, 1–12. https://doi.org/10.1109/TGRS.2024.3422171.

Zhang, D., Zhang, L., Dong, J., Wang, Y., Yang, C., Liao, M., 2024. Improved phase gradient stacking for landslide detection. Landslides 21, 1829–1847. https://doi.org/10.1007/s10346-024-02263-3.

Zhang, Y., Fattahi, H., Amelung, F., 2019. Small baseline InSAR time series analysis: unwrapping error correction and noise reduction. Comput. Geosci. 133, 104331. https://doi.org/10.1016/j.cageo.2019.104331.

Zheng, W., Hu, J., Lu, Z., Hu, X., Sun, Q., Liu, J., Huang, B., 2024. Enhancing 4-D landslide monitoring and block interaction analysis with a novel Kalman-filter-based InSAR approach. JGR Earth Surface 129, e2024JF007923. https://doi.org/10.1029/2024JF007923.

Zwieback, S., Meyer, F.J., 2021. Repeat-pass interferometric speckle. IEEE Trans. Geosci. Remote Sensing 59, 6736–6750. https://doi.org/10.1109/TGRS.2020.3029991.